SANDIA REPORT
SAND2020-10743
Printed September, 2020

Sandia National Laboratories

Theoretical study of various nonlinear phenomena in plasma systems and scaling of magneto-inertial-fusion targets

D. E. Ruiz

Prepared by
Sandia National Laboratories
Albuquerque, New Mexico 87185
Livermore, California 94550

Issued by Sandia National Laboratories, operated for the United States Department of Energy by National Technology & Engineering Solutions of Sandia, LLC.

Available to DOE and DOE contractors from

U.S. Department of Energy
Office of Scientific and Technical Information
P.O. Box 62
Oak Ridge, TN 37831

Telephone: (865) 576-8401
Facsimile: (865) 576-5728
E-Mail: reports@osti.gov
Online ordering: http://www.osti.gov/scitech

Available to the public from

U.S. Department of Commerce
National Technical Information Service
5301 Shawnee Road
Alexandria, VA 22312

Telephone: (800) 553-6847
Facsimile: (703) 605-6900
E-Mail: orders@ntis.gov
Online order: https://classic.ntis.gov/help/order-methods

ABSTRACT

Plasma physics is an exciting field of study with a wide variety of nonlinear processes that come into play. Examples of such processes include the interaction of small-scale turbulence with large-scale plasma structures and the nonlinear saturation of plasma instabilities, for example those of magneto-hydrodynamical nature. During this Truman LDRD project, I studied a collection of nonlinear problems that are of interest to the field of plasma physics. This LDRD report summarizes four main research accomplishments.

First, a new statistical model for describing inhomogeneous drift-wave turbulence interacting with zonal flows was developed. This new model includes the effects of nonlinear wave–wave collisions, which are expected to change the spectrum of the underlying DW turbulence and therefore the generation of zonal flows.

Second, a new mathematical formalism was proposed to systematically apply the nonlinear WKB approximation to general field theories, including those often used in fluid dynamics. This formalism represents an interesting tool for studying physical systems that show an explicit scale separation.

Third, a weakly nonlinear model was developed to describe the magneto-Rayleigh–Taylor instability. This instability is of paramount importance to understand as it can reduce the performance of magnetic-inertial-fusion (MIF) platforms. The developed models captures the effects of harmonic generation and saturation of the linear growth of the instability.

Finally, a framework was proposed for scaling magneto-inertial fusion (MIF) targets to larger pulsed-power drivers. From this framework, a set of scaling rules were derived that conserve the physical regimes of MIF systems when scaling up in peak current. By doing so, deleterious nonlinear processes that affect MIF performance may be kept at bay.

ACKNOWLEDGMENT

I first want to thank Sandia National Laboratories and, in particular, the LDRD office for providing the excellent opportunity of the Truman Fellowship. During the last three years as a Truman Fellow, I was the lead investigator of my own research project. Overall, the experience was really amazing. The intellectual freedom of the fellowship permitted me to tackle problems that were aligned to my own research interests and to the stockpile stewardship mission of the laboratory. Undoubtedly, the Truman Fellowship allowed me to expand my research in several directions that go beyond what I was doing in graduate school. I am also particularly grateful that, as a Truman Fellow, I was able to take a step back and invest time to expand my research "toolkit." Examples include becoming more proficient in computer coding, learning about differential geometry, and gaining experience to run one of the big laboratory production codes. I am sure that the new tools that I have acquired during these past three years have not only made me a better scientist but will also be useful for the rest of my research career.

I am also grateful for the time and support that the managers of my home organization 1684 have provided me. Perhaps unexpectedly, during the last three years, our organization has had four managers serving in different capacities (both interim and permanent). I benefited from each one of their unique styles of leadership and communication. I foremost want to thank Kyle Peterson, who was my manager during my arrival to Sandia and throughout the majority of my fellowship tenure. Kyle's initial and enthusiastic support was undoubtedly a key factor to submit strong application for the fellowship. I am particularly thankful to Kyle for his time to talk to me as I underwent the steep transition from a graduate student to an independent principle investigator with his own project. I also thank him for indoctrinating me on the overall stockpile-stewardship mission of the laboratory and for helping me navigate the clearance process. After Kyle left the management position of 1684, Thomas Mattsson and Stephanie Hansen each took the interim roles as managers of our organization. Although their tenures were brief, they undoubtedly had a great impact in my early career as a Sandian. Although Thomas also became one of my mentors (more on that later), I am particularly grateful to him as a manager for overseeing my long-awaited move to an office space in 960. This detail might be small, but the close proximity to my work colleagues has only increased my enjoyment of my work at Sandia, as well as my productivity and collaboration with others. I want to thank Stephanie for her service to volunteer as interim manager of our organization. I am particularly grateful to Stephanie for helping me take the next step in my career as I transitioned from a Truman Fellow to a permanent staff member at Sandia. I also thank Stephanie for being an excellent leader during the early stages of the ongoing COVID-19 crisis. Her timely updates on recent developments regarding lab policies and her sincere curiosity on how we were navigating these difficult times were infinitely helpful. I finally want to thank Kris Beckwith, who has only recently filled the management position

of 1684. Kris undeniably has strong technical background in theoretical and computational physics. I am looking forward to working with him as my fellowship tenure comes to an end and I join the main rank and file of Sandia's members of the technical staff.

I would like to specially thank my mentors Michael Glinsky, Thomas Mattsson, and Paul Schmit for their continuous guidance throughout these past few years. In particular, I thank Michael for his enthusiasm to have me submit an application for the Truman Fellowship. I thank him for welcoming me to Sandia and for being an initial guide on how things work around here. I also thank him for our collaboration during the first half of my fellowship.

I thank my mentor and friend, Thomas Mattsson. Through our interactions in the office and on our bikes, Thomas has been an invaluable resource to learn more about the importance of our mission outside ICF. I thank him for his time and openness to talk about the problems that I was working on. I also thank him for his encouragement to tackle problems that are relevant to our center and for his support to complete the current-scaling work.

I am particularly grateful to my mentor, collaborator, and friend, Paul Schmit. First, I want to thank Paul for his encouragement and guidance as I prepared my proposal for the Truman Fellowship. I also thank him for our numerous conversations and our Friday lunch outings, where we would talk about general physics and interesting problems to work on. I particularly appreciate his invitation to collaborate with him on the current-scaling work. It is hard to quantify how much I have benefited from this project. In short, it has been a great opportunity to quickly learn about the physics concerning MIF and to contribute in an important way to our center's scaling story for the next pulsed-power machine. Paul has taught me that it is possible to be an excellent theorist while also being a successful target designer. His passion for the mission and his incredible work ethic only inspire me to strive to do the same with my own career at Sandia.

I also would like to sincerely thank another of my closest collaborators, David Yager-Elorriaga. I admire David's passion for the experimental study of interfacial-hydrodynamical instabilities in high-energy density (HED) systems. David introduced me to the problem of the magneto Rayleigh–Taylor instability. Working with David has been another big opportunity to bring my research closer to the main research activities in our center. It has been a pleasure working with him on this domain and on MagLIF current scaling. I think that we are a good experimentalist–theoretist team, and I am looking forward to continue to collaborate with him in the future.

I want to specially thank Matt Weis for his time and infinite patience to teach me how to use the radiation-magnetohydrodynamics code HYDRA. Given that I had no prior experience with big production codes, it is worth noting that Matt had to teach me the very basics from submitting jobs to Sandia's clusters to visualizing HYDRA outputs. When I struggle with HYDRA problems, Matt has been an excellent resource to ask questions, and he has gladly shared the secrets of the trade concerning remeshing strategies. I thank him for kindly giving me some of his decks which without any doubt have helped me overcome much faster the learning curve and to become more productive with the code. On the research

side, it has been fun working with him, and I thank him for the various collaborations that we have engaged on regarding laser preheat in MagLIF.

I would also like to thank several people in 960 with whom I have interacted throughout my fellowship. I particularly want to thank Jeff Fein for his friendship and for our insightful conversations regarding general LPI phenomena. I am grateful to Chris Jennings for his many useful suggestions regarding numerical modeling of magnetically-driven implosions and for his general insights to the physics of our MIF experiments. I thank Stephanie Hansen for our interesting discussions on atomic physics. I specially thank Edmund Yu, who has always championed that I remain faithful to who I am as a scientific researcher and to find ways to use my abilities to best contribute to the center. I want to thank Pat Knapp for our conversations concerning Bayesian analysis of MagLIF data and the interesting details of the Decel data. I thank Adam Harvey-Thompson for our several research collaborations on MagLIF preheat. Finally, I thank Nicky Bennett for reviewing this report after submitting it to the R&A process.

I also want to thank Dave Ampleford, who was the program manager who oversaw my first design cycle for a MagLIF experiment. I sincerely appreciate his trust on me to design the 2020 MagLIF current-scaling series. Sometimes you need to throw a kid in the water so that he learns how to swim. In some ways, I believe that this was my situation. Nevertheless, I am glad that this happened: I came out of the process with a deeper understanding of how MagLIF works and with renewed confidence that I can tangibly contribute to our center's day-to-day research thrusts.

Finally, I want to specially thank Yolanda Moreno for being the liaison for the Truman Fellows and for her general kindness as a person. I also want to thank my direct senior managers, whose strong support for the current-scaling work undoubtedly provided a strong motivation to deliver one's best for the project. In this regard, I thank my Level 2 manager, Greg Rochau. I also want to thank our previous center director Kieth Matzen, who welcomed me when I arrived to Sandia, and to our current center director Dan Sinars, who like Greg, has shown enormous support for the current-scaling work.

I finally want to thank my external collaborators: Ilya Dodin, Josh Burby, and Sasha Velikovich. Ilya Dodin was my thesis advisor during graduate school. During the first year of my Fellowship, we worked on finishing some pending projects related to my thesis. My work with Josh Burby on variational principles for nonlinear-WKB systems was intellectually stimulating and rewarding. Although we have not started yet a formal collaboration together, I also want to thank Sasha Velikovich. Sasha has been a great resource of knowledge on previous work done on hydrodynamical instabilities. I particularly appreciate him hosting me for a week-long visit at NRL and for his enthusiasm on the new techniques that I am advocating to study hydrodynamical instabilities.

CONTENTS

LIST OF FIGURES

LIST OF TABLES

SUMMARY

Throughout this LDRD project, I had the pleasure of participating on a wide variety of research projects whose topics included the growth of hydrodynamical instabilities in accelerating systems, the study of laser propagation inside plasmas, the generation of mean-field structures from small-scale plasma turbulence, and the growth of interfacial instabilities in hydrodynamic systems. A list of the main publications that I have co-authored during the three-year tenure of the Truman Fellowship is provided below. A list of invited colloquium talks given is also provided at the end.

Papers in preparation

1. **D. E. Ruiz**, D. A. Yager-Elorriaga, D. B. Sinars, K. J. Peterson, and M. R. Weis, *"Harmonic generation and inverse-cascade processes in the Z-pinch driven, multimode magneto Rayleigh–Taylor instability,"* in preparation.
2. **D. E. Ruiz**, P. F. Schmit, D. A. Yager-Elorriaga, and M. R. Weis, *"Increasing stability and maintaining performance of magneto-inertial fusion targets via self-similar scaling strategies,"* in preparation.

Submitted papers

1. A. J. Harvey-Thompson, M. R. Weis, **D. E. Ruiz**, M. S. Wei, A. B. Sefkow, T. Nagayama, E. M. Campbell, J. A. Fooks, M. E. Glinsky, and K. J. Peterson, *"The effect of laser entrance hole foil thickness on MagLIF-relevant laser preheat,"* submitted to Phys. Plasmas.
2. M. R. Weis, A. J. Harvey–Thompson, and **D. E. Ruiz**, "MHD modeling of laser preheat in MagLIF," submitted to Phys. Plasmas.

Published/accepted papers

1. P. F. Knapp, M. R. Martin, D. Yager-Elorriaga, A. J. Porwitzky, F. W. Doss, G. A. Shipley, C. A. Jennings, **D. E. Ruiz**, T. Byvank, C. C. Kuranz, C. E. Myers, D. H. Dolan, K. Cochrane, M. Schollmeier, I. C. Smith, T. R. Mattsson, B. M. Jones, K. Peterson, J. Schwarz, R. D. McBride, D. G. Flicker, and D. B. Sinars, *"A Novel, Magnetically Driven Convergent Richtmyer-Meshkov Platform,"* Phys. Plasmas **27**, 092707

(2020). **(This work was chosen as an Editor's choice article for the month of September 2020.)**

2. M. R. Gomez, S. A. Slutz, C. A. Jennings, D. J. Ampleford, M. R. Weis, C. E. Myers, D. A. Yager-Elorriaga, K. D. Hahn, S. B. Hansen, E. C. Harding, A. J. Harvey-Thompson, D. C. Lamppa, M. Mangan, P. F. Knapp, T. J. Awe, G. A. Chandler, G. W. Cooper, J. R. Fein, M. Geissel, M. E. Glinsky, W. E. Lewis, C. L. Ruiz, **D. E. Ruiz**, M. E. Savage, P. F. Schmit, I.C. Smith1, J.D. Styron, J. L. Porter, B. Jones, T. R. Mattsson, K. J. Peterson, G. A. Rochau, D. B. Sinars, *"Performance scaling in magnetized liner inertial fusion experiments,"* accepted in Phys. Rev. Lett. (2020).

3. M. A. Oancea, J. Joudioux, I. Y. Dodin, **D. E. Ruiz**, C. F. Paganini, and L. Andersson, *"The gravitational spin Hall effect of light,"* Phys. Rev. D **102**, 024075 (2020).

4. P. F. Schmit and **D. E. Ruiz**, *"A conservative approach to scaling magneto-inertial fusion concepts to larger pulsed-power drivers,"* Phys. Plasmas **27**, 062707 (2020). **(This work was chosen as an Editor's choice article for the month of July 2020.)**

5. J. W. Burby and **D. E. Ruiz**, *"Variational nonlinear WKB in the Eulerian frame,"* J. Math. Phys. **61**, 053101 (2020).

6. **D. E. Ruiz**, *"On a variational formulation of the weakly nonlinear magnetic Rayleigh–Taylor instability,"* Phys. Plasmas **27**, 022121 (2020).

7. I. Y. Dodin, **D. E. Ruiz**, K. Yanagihara, Y. Zhou, and S. Kubo, *"Quasioptical modeling of wave beams with and without mode conversion: I. Basic theory,"* Phys. Plasmas **26**, 072110 (2019).

8. **D. E. Ruiz**, M. E. Glinsky, and I. Y. Dodin, *"Wave kinetic equation for inhomogeneous drift-wave turbulence beyond the quasilinear approximation,"* J. Plasma Phys. **85**, 905850101 (2019).

9. P. F. Knapp, M. R. Gomez, S. B. Hansen, M. E. Glinsky, C. A. Jennings, S. A. Slutz, E. C. Harding, K. D. Hahn, M. R. Weis, M. Evans, M. R. Martin, A. J. Harvey-Thompson, M. Geissel, I. C. Smith, **D. E. Ruiz**, K. J. Peterson, B. M. Jones, J. Schwarz, G. A. Rochau, D. B. Sinars, R. D. McBride, and P. A. Gourdain, *"Origins and effects of mix on magnetized liner inertial fusion target performance,"* Phys. Plasmas **26**, 012704 (2019).

10. A. J. Harvey-Thompson, M. R. Weis, E. C. Harding, M. Geissel, D. J. Ampleford, G. A. Chandler, J. R. Fein, M. E. Glinsky, M. R. Gomez, K. D. Hahn, S. B. Hansen, C. A. Jennings, P. F. Knapp, R. R. Paguio, L. Perea, K. J. Peterson, J. L. Porter, P. K. Rambo, G. K. Robertson, G. A. Rochau, **D. E. Ruiz**, J. Schwarz, J. E. Shores, D. B. Sinars, S. A. Slutz, G. E. Smith, I. C. Smith, C. S. Speas, and K. Whittemore, *"Diagnosing and mitigating laser preheat induced mix in MagLIF,"* Phys. Plasmas **25**, 112705 (2018).

11. H. Zhu, Y. Zhou, **D. E. Ruiz**, and I. Y. Dodin, *"Wave kinetics of drift-wave turbulence and zonal flows beyond the ray approximation,"* Phys. Rev. E **97**, 053210 (2018).

12. I. Y. Dodin, **D. E. Ruiz**, and S. Kubo, *"Mode conversion in cold low-density plasma with a sheared magnetic field,"* Phys. Plasmas **24**, 122116 (2017).

Invited talks and colloquia

1. *"On a variational formulation of the weakly nonlinear magnetic-Rayleigh–Taylor instability,"* Naval Research Laboratory, Washington, DC, September 18, 2019.

2. *"Describing drift-wave turbulence from a phase-space perspective,"* Mathematics Department, University of Missouri, Columbia, MO, March 6, 2019.

3. *"Wave kinetic equation in a nonstationary and inhomogeneous medium with a weak quadratic nonlinearity,"* Courant Institute, New York City, NY, February 20, 2018.

NOMENCLATURE

Table 0-1. List of acronyms used thorughout this report.

Abbreviation	Definition
AR	Aspect ratio
DIA	Direct interaction approximation
DT	Deuterium Tritium
DW	Drift wave
HED	High Energy Density
IFAR	In-flight aspect ratio
ITC	Implosion-time conserving
ITC-r	Implosion-time, radiation conserving
ITC-t	Implosion-time, temperature conserving
LPI	Laser–plasma interactions
MagLIF	MAGnetized Liner Inertial Fusion
MIF	Magneto Inertial Fusion
MFE	Magnetic fusion experiments
MHD	Magneto-hydrodynamic
MRT	Magnetic Rayleigh–Taylor
MRTI	Magnetic Rayleigh–Taylor instability
MSR	Martin Siggia Rose
NL-WKB	Nonlinear Wentzel–Kramer– Brillouin
RMC	Realizable Markovian Closure
PDE	Partial differential equation
RT	Rayleigh–Taylor
SA	Saturation amplitude
WKB	Wentzel Kramers Brillouin
WKE	Wave kinetic equation
wNL	Weakly nonlinear
WWT	Weak wave turbulence
ZF	Zonal flow

1. INTRODUCTION

This Truman LDRD project was focused on studying a collection of problems of nonlinear nature that are of interest in the field of plasma physics. This report summarizes the main research accomplishments that were obtained during this project. The following chapters will discuss four different projects in which I played a lead role. Each chapter is intended as a summary of each project. The chapters provide the context and motivation behind the research, they clearly state the main results obtained, and they discuss avenues of future research that could be pursued as follow-up work. The results from these projects were published in peer-reviewed journals. Some excerpts from these publications were used when compiling the results for this report.

To provide further guidance to the reader, I summarize below the contents of each chapter. It is worth mentioning that the chapters are independent from one another. Therefore, if the reader finds a particular topic interesting, he or she can immediately refer to the corresponding chapter of interest without having to read the previous material in the report.

In Chapter 2, I discuss my work on the formation of large-scale zonal flows (ZFs) from inhomogeneous, small-scale drift-wave (DW) turbulence. ZFs are present in magnetic fusion devices and in planetary atmospheres. The spontaneous formation of ZFs is often described using statistical theories derived within the quasilinear approximation. In this regard, the two main workhorse models are the second-order cumulant expansion (also known as CE2) and the wave kinetic equation. However, the quasilinear approximation neglects wave–wave collisions. Hence, some important effects such as the Batchelor–Kraichnan inverse-energy cascade are not captured within this approximation. In this project, we developed a wave kinetic equation that includes a DW collision operator in the presence of zonal flows. The obtained collision operator conserves both the total enstrophy and energy of the system. In this chapter, I shall present the main results obtained, as well as preliminary unpublished simulations using this new formalism. The published results of this research are found in Ref. [1].

In Chapter 3, I present a new mathematical formalism that was developed to elegantly marry the nonlinear WKB approximation with general field theories, including those often used in fluid dynamics. Nonlinear WKB is a multiscale technique for studying locally-plane-wave solutions of nonlinear partial differential equations (PDEs). Its application comprises two steps: (1) replacement of the original PDE with an extended system separating the large scales from the small, and (2) reduction of the extended system to its slow manifold. In the first part of this work, we provided a systematic method for replacing field theories, in which their action functionals were known, with their nonlinear WKB-extended counterparts. In the second part of this work, we show that variational fluid theories with particle relabeling symmetry can be adapted so that a nonlinear WKB extension can be introduced while

remaining in the Eulerian frame for the fluid description. As an illustrative example, we use our results to systematically deduce a variational model of high-frequency acoustic waves interacting with a larger-scale compressible isothermal flow. Additional details on results from this work are found in Ref. [2].

In Chapter 4, I discuss my work on developing a weakly nonlinear model for the magneto-Rayleigh–Taylor instability. The magnetic-Rayleigh–Taylor (MRT) instability is a ubiquitous phenomenon that occurs in magnetically-driven Z-pinch implosions. It is important to understand this instability since it can decrease the performance of such implosions. In this work, I proposed a theoretical model for the weakly nonlinear MRT instability that was derived by asymptotically expanding an action principle for the nonlinear MRT instability. The resulting theory captures the harmonic generation of MRT modes. It is shown that the amplitude at which the linear magnetic-Rayleigh–Taylor instability exponential growth saturates depends on the stabilization effect of the magnetic-field tension. Overall, the theory provides an intuitive interpretation of the weakly nonlinear MRT instability and provides a systematic approach for studying this instability in more complex settings. The results from this work were published in Ref. [3].

In Chapter 5, I discuss the development of a new framework for scaling magneto-inertial fusion (MIF) targets to larger pulsed-power drivers. The Magnetized Liner Inertial Fusion (MagLIF) experimental platform represents the most successful demonstration of MIF techniques for pursuing fusion in the laboratory. However, it is unclear how to scale MIF concepts like MagLIF to more powerful pulsed-power drivers while avoiding significant changes in physical regimes that could adversely impact performance. In this work, we propose a conservative approach for scaling general MIF implosions, including MagLIF. The framework is based on a simple model describing a thin, current-driven, cylindrical shell that compresses a preheated, adiabatic fuel. By imposing that scaled implosions remain self-similar, we obtain a set of scaling rules expressing key target design parameters and performance metrics as functions of the maximum driver current $I_{\max}$. We identify several scaling paths offering unique, complementary benefits and trade-offs in terms of physics risks and driver requirements. In the absence of alpha heating, our scaling paths exhibit neutron yield per-unit-length scaling as $\hat{Y} \propto [I_{\max}^3, I_{\max}^{4.14}]$ and ignition parameter scaling as $\chi \propto [I_{\max}, I_{\max}^{2.14}]$. Results of this work were published in Ref. [4].

2. WAVE KINETIC EQUATION FOR INHOMOGENEOUS DRIFT-WAVE TURBULENCE BEYOND THE QUASILINEAR APPROXIMATION

2.1. Introduction

The interaction between drift-wave (DW) turbulence and zonal flows (ZFs) has been widely studied in plasma physics [5; 6; 7; 8; 9; 10; 11]. In the context of magnetic fusion experiments (MFE) [6; 12; 13], the spontaneous emergence of ZFs significantly affects the transport of energy, momentum, and particles (see Fig. 2-1). Understanding this phenomenon is critical to improving plasma confinement, but modeling the underlying physics remains difficult. For example, direct numerical simulations of interacting DWs and ZFs strongly depend on the initial conditions and the external random forcing. Moreover, to obtain meaningful conclusions, numerous direct numerical simulations are needed to collect the minimum statistics required. Therefore, statistical methods represent a useful alternative and are widely applied in the DW-turbulence research, even at the cost of introducing approximations.

The modeling of homogeneous turbulence via statistical models has a long history. Perhaps the simplest model is weak wave turbulence (WWT) theory [15]. In WWT theory, the main object of study is the wave collision operator and the steady-state spectra that it generates. From this model, the power law for the Batchelor–Kraichnan inverse-energy cascade can been deduced. Although WWT theory is intuitive, it does have its downsides, for example, it cannot capture the effects of resonance broadening in a self-consistent manner [15]. To remedy this, other more advanced statistical closures have been developed to solve this problem. Examples include the Direct Interaction Approximation (DIA) [16], the Realizable Markovian Closure (RMC) [17], and the Martin–Siggia–Rose (MSR) formalism [18]. However, these more advanced theories cannot describe inhomogeneous turbulence, where DW propagate in a plasma that has spatial dependencies. This setting is of particular interest when studying DWs interacting with ZFs.

To model the interaction of DWs and ZFs, one particular statistical approach is the so-called quasilinear (QL) approximation [19], where the ZF equation is kept nonlinear and the equation for DWs is linearized. This approximation effectively neglects the nonlinear interactions between the DWs (which is the key element of homogeneous turbulence) and only retains the nonlinear interaction with the ZFs. It is generally thought that ignoring such wave–wave interactions is appropriate when specifically studying the emergence of zonal flows. Within the quasilinear approximation, there exists multiple statistical formalisms. Among these, the most accurate are the second-order cumulant expansion (CE2) [19; 20; 21; 22; 23] and the Wigner–Moyal [24; 25; 26; 27] formalisms. These theories do not assume a scale separation between the DWs and ZFs, and they give the most accurate results within

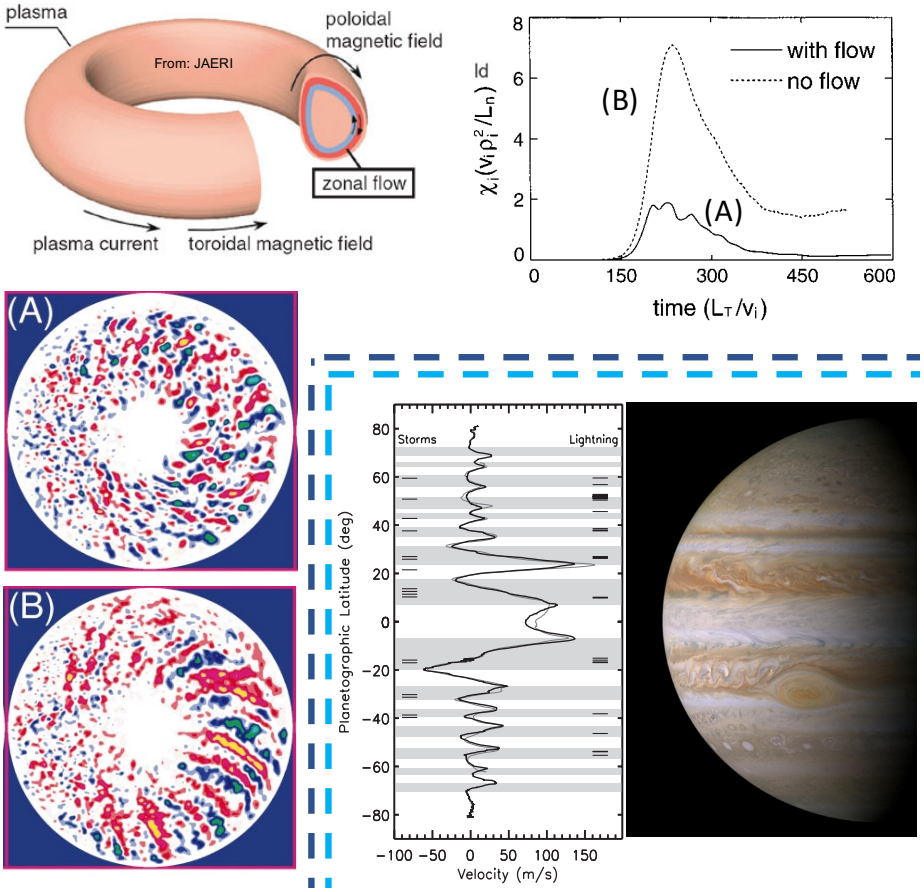

Figure 2-1. Zonal flows are present in magnetic fusion experiments and in planetary atmospheres. Understanding their interactions with small-scale turbulence is essential to understand. As an example, when ZFs emerge in tokamaks, they are known to suppress the ion heat conduction, as shown in the top-right corner of the figure. Also, ZFs are known to reduce the magnitude of small-scale turbulence as shown in the bottom-left corner. (Images are taken from Refs. [7; 14].)

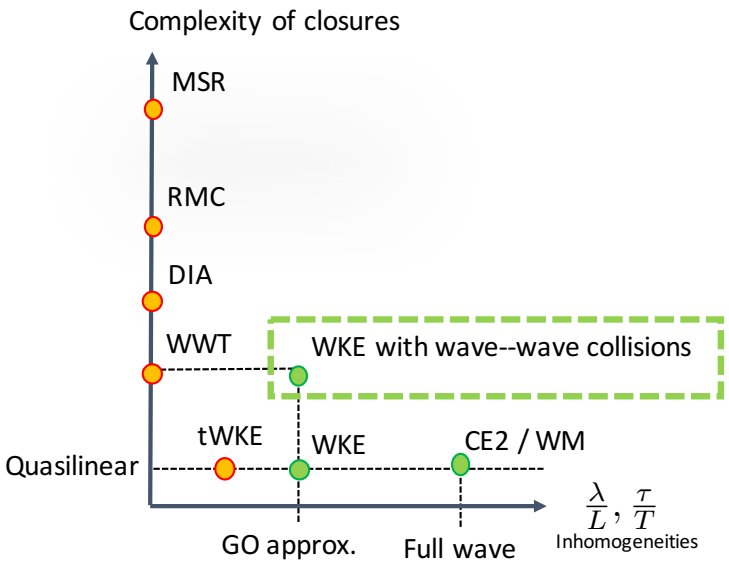

Figure 2-2. Schematic diagram portraying the various statistical models for modeling DW turbulence. Along the x axis, models are ordered according to how they deal with inhomogeneities in the plasma. To be more specific, models sitting on the $x = 0$ axis do not consider inhomogeneities. The CE2 and WM formalisms do not assume any scale separation; therefore, they are placed on the right of the diagram. Along the y axis, models are ordered according to the complexity of the statistical closure. Quasilinear theory is placed on the bottom since it neglects nonlinear wave–wave interactions among the DWs. The most complete formalism in terms of the statistical closure involved is the Martin–Siggia–Rose (MSR) description. The work discussed in this chapter added nonlinear wave–wave collisions to the wave-kinetic-equation description.

the quasilinear approach. However, they do involve PDEs which are nonlocal in nature, and therefore the underlying physical interpretation can be somewhat obscured.

Another popular quasilinear approach is the wave kinetic equation (WKE) model [28; 24; 25; 29; 30; 5; 31; 32; 33; 34; 35; 36; 37; 38; 39]. In this framework, the DW are assumed to be of smaller scale compared to the larger-scale zonal flows. By introducing an explicit scale separation, it is possible to invoke the geometrical-optics approximation and to localize the CE2 and Wigner–Moyal formalisms [28; 24]. Although the WKE-based description may miss some physics [40] that the CE2 and WM theories do capture, the WKE has the intuitive form of a Liouville equation for the DW action density J in the ray phase space [28; 24; 25; 29; 40]:

$$\partial_t J + \{J, \Omega\} = 2\Gamma J, \tag{2.1}$$

where J is the DW action density, Ω is the local DW frequency, Γ is a dissipation rate due to interactions with ZFs, and $\{\cdot, \cdot\}$ is the canonical Poisson bracket. (For the sake of clarity, terms related to external forcing and dissipation are omitted here.) In this description, DW intuitively propagate in a ray phase-space and are absorbed when a ZF emerges. The last term found in Refs. [28; 24] is essential to conserve energy and enstrophy in the system.

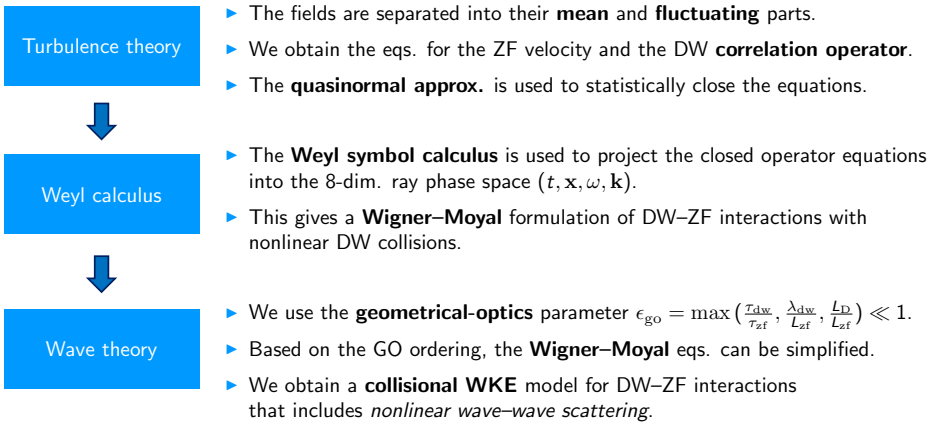

Figure 2-3. The calculation of a collisional wave-kinetic-equation model for describing the interaction between DWs and ZFs required combining elements from turbulence theory, the phase-space Weyl calculus, and general wave theory, in particular geometrical optics.

However, as with all quasilinear models, Eq. (2.1) neglects nonlinear wave–wave scattering, and in consequence, is not able to capture the Batchelor–Kraichnan inverse-energy cascade [22] or produce the Kolmogorov–Zakharov spectra for DWs [11]. If the DW spectrum is modified due to the presence of collisions, it is entirely possible that the ensuing interaction with ZFs may be altered. Hence, a question remains as to whether the existing WKE for inhomogeneous turbulence can be complemented with a wave–wave collision operator $C[J, J]$.

Under the auspices of the Truman Fellowship, the theory of DW–ZF interactions was expanded by explicitly calculating the wave–wave collision operator $C[J, J]$ for DWs. Strictly speaking, this operator had been derived before for the case of homogenoeus turbulence [11]. However, the goal of this project was to derive it for the case of inhomogeneous DW turbulence under the umbrella of the wave-kinetic-equation formalism. A diagram of how this work fits into the general DW-ZF turbulence theory is shown in Fig. 2-2. The main results of this work were published in Ref. [1].

2.2. Main result: Derivation of a wave-kinetic-equation model with nonlinear wave–wave collisions included

Broadly speaking, our work combined elements from homogeneous turbulence theory [15], the Weyl symbol calculus [41; 42; 43], and general wave theory, in particular geometrical optics [44; 45; 46]. Below, I shall summarize the main steps in the paper.

The starting point of the calculation was the generalized Hasegawa–Mima equation (gHME) [47; 31]. Based on homogeneous weak-wave-turbulence (WWT) theory [15], we separated the main dynamical variable, the electric potential ψ, into its mean and fluctuating components. The mean part of the potential was associated to the large-scale, slowly-varying

ZF fields, while the fluctuating component was associated to the small-scale, DW turbulence. To construct a statistical theory, a two-point correlation operator $\hat{W} = \langle\langle |\widetilde{w}\rangle \langle\widetilde{w}| \rangle\rangle$ for the DWs was introduced, where $\widetilde{w}$ is a fluctuating electrostatic vorticity and $\langle\langle\cdot\rangle\rangle$ is some averaging method. We preferred to work with the abstract operator $\hat{W}$ as it was coordinate free, and therefore many of the ensuing calculations were able to be computed symbolically. As it is usual with statistical theories, the introduction of correlation operator lead to the well-known closure problem, where equations are always needed to be found for the higher-order moments. To statistically close the equations, we utilized the quasinormal approximation, which is related to the random-phase approximation. This statistical closure captures the leading-order nonlinear DW collisions. As a testament of the various manipulations involved in these calculations, the coordinate-free governing equation for the correlation operator was found to be

$$[\widehat{\mathcal{D}}_{\mathrm{H}}, \widehat{\mathcal{W}}]_- + i[\widehat{\mathcal{D}}_{\mathrm{A}}, \widehat{\mathcal{W}}]_+ = 2i\epsilon_{\mathrm{nl}}^2 \big[\widehat{\mathcal{F}}\,(\widehat{\mathcal{D}}^{-1})^\dagger\big]_{\mathrm{A}} - 2i\epsilon_{\mathrm{nl}}^2 \big[\widehat{\eta}\,\widehat{\mathcal{W}}\big]_{\mathrm{A}} + 2i\epsilon^2 \big[\widehat{\mathcal{S}}(\widehat{\mathcal{D}}^{-1})^\dagger\big]_{\mathrm{A}}, \tag{2.2}$$

where $[\cdot,\cdot]_\pm$ are the symmetric and antisymmetric commutation brackets, $\widehat{\mathcal{D}}_{\mathrm{H}}$ is the Hermitian part of the DW dispersion operator, $\widehat{\mathcal{D}}_{\mathrm{A}}$ is the corresponding anti-Hermitian part, and $\widehat{\mathcal{S}}$ is a source term for the DW fluctuations. The small parameters ϵ_{nl} and ϵ_{go} are simply ordering parameters, whose meaning is not necessary to explain. The operators $\widehat{\mathcal{F}}$ and $\widehat{\eta}$ depend nonlinearly on the two-point correlation operator $\widehat{\mathcal{W}}$. These operators act as the nonlinear coupling terms that are usually encountered in WWT theory. From these, the DW collisional operator emerges. These operators are symbolically written as

$$\widehat{\eta} \doteq -\int \mathrm{d}^3\mathsf{x}\,\mathrm{d}^3\mathsf{y}\;|\,\mathsf{x}\,\rangle\,\langle\,\mathsf{y}\,|\,(\widehat{\mathcal{D}}^{-1})^\dagger \widehat{\mathcal{K}}(\mathsf{x})\,\widehat{\mathcal{W}}\,\widehat{\mathcal{K}}^\dagger(\mathsf{y}), \tag{2.3}$$

$$\widehat{\mathcal{F}} \doteq \frac{1}{2}\int \mathrm{d}^3\mathsf{x}\,\mathrm{d}^3\mathsf{y}\;|\,\mathsf{x}\,\rangle\,\langle\,\mathsf{y}\,|\,\mathrm{Tr}[\,\widehat{\mathcal{K}}(\mathsf{x})\,\widehat{\mathcal{W}}\,\widehat{\mathcal{K}}^\dagger(\mathsf{y})\,\widehat{\mathcal{W}}\,], \tag{2.4}$$

where $\widehat{\mathcal{K}}$ is some coupling kernel.

The result in Eqs. (2.2)–(2.4) is general and coordinate free. However, in order to do a practical calculation, it was necessary to project these equations into a coordinate space. For inhomogeneous turbulence, it is often convenient to project the dynamics of the correlation operator onto the extended ray phase space $(\omega, t, \mathbf{x}, \mathbf{k})$, where ω is the wave frequency and $\mathbf{k}$ is the wavevector [24; 25; 40; 30]. As first shown in Ref. [24], the projection to the extended phase space can be done systematically using the Weyl symbol calculus [41; 42; 43]. This procedure lead to an equation that governs the dynamics of the Wigner function $W(\omega, t, \mathbf{x}, \mathbf{k})$ describing the DW fluctuations. The Wigner function is formally defined as [42]

$$\begin{aligned} W(t,\mathbf{x},\omega,\mathbf{k}) &= \int \mathrm{d}t'\,\mathrm{d}^3\mathbf{x}'\,e^{i(\omega s-\mathbf{k}\cdot\mathbf{x}')/\epsilon}\,\langle\,t+\tfrac{1}{2}t',\mathbf{x}+\tfrac{1}{2}\mathbf{x}'\,|\,\widehat{\mathcal{W}}\,|\,t-\tfrac{1}{2}t',\mathbf{x}-\tfrac{1}{2}\mathbf{x}'\,\rangle \\ &= \int \mathrm{d}t'\,\mathrm{d}^3\mathbf{x}'\,e^{i(\omega s-\mathbf{k}\cdot\mathbf{x}')/\epsilon}\langle\!\langle \tilde{w}\left(t+\tfrac{1}{2}t',\mathbf{x}+\tfrac{1}{2}\mathbf{x}'\right)\tilde{w}\left(t-\tfrac{1}{2}t',\mathbf{x}-\tfrac{1}{2}\mathbf{x}'\right)\rangle\!\rangle. \end{aligned} \tag{2.5}$$

At this point, even though the abstract Eq. (2.2) was projected into a phase-space, the resulting Wigner–Moyal equation was still hopelessly complicated since it is a pseudo-differential equation. In other words, it is a partial differential equation of infinite order!

To remedy this situation, it was necessary to reduce the order of the governing PDE. This was done by assuming that there is a temporal and spatial scale separation between the DW and ZF fields. Specifically, let $\tau_{\rm dw}$ and $\lambda_{\rm dw}$ respectively denote the characteristic period and wavelength of the DWs. In a similar manner, the characteristic time and length scales of the ZFs are given by $T_{\rm zf}$ and $L_{\rm zf}$, respectively. The scale separation between DWs and ZFs is characterized by the geometrical-optics (GO) parameter

$$\epsilon_{\rm go} \doteq \max\left(\frac{\tau_{\rm dw}}{T_{\rm zf}}, \frac{\lambda_{\rm dw}}{L_{\rm zf}}\right) \ll 1. \tag{2.6}$$

Introducing a scale-separation ordering allowed to neglect the higher-order derivatives appearing in the Wigner–Moyal equation. The final result was a wave kinetic equation that contained a wave–wave collision operator [1].

The obtained model for DW–ZF interactions is the following. The equations for the wave action density $J(t,y,\mathbf{k})$ for the DW fluctuations and of the ZF velocity field $U(t,y)$ are

$$\partial_t J + \{J,\Omega\} = -2\mu_{\rm dw} J + 2\Gamma J + S_{\rm ext} + \epsilon\, C[J,J], \tag{2.7}$$

$$\partial_t U + \mu_{\rm zf} U = \epsilon^2 \frac{\partial}{\partial y} \int \frac{{\rm d}^2\mathbf{k}}{(2\pi\epsilon)^2} \frac{k_x k_y}{k_{\rm D}^4} J(t,y,\mathbf{k}). \tag{2.8}$$

where $\{\cdot,\cdot\} = \overleftarrow{\partial}_{\mathbf{x}} \cdot \overrightarrow{\partial}_{\mathbf{k}} - \overleftarrow{\partial}_{\mathbf{k}} \cdot \overrightarrow{\partial}_{\mathbf{x}}$. The wave frequency Ω and dissipation term Γ are given by

$$\Omega(t,y,\mathbf{k}) \doteq k_x U - (\beta - U'')k_x/k_{\rm D}^2, \tag{2.9a}$$

$$\Gamma(t,y,\mathbf{k}) \doteq -U''' k_x k_y / k_{\rm D}^4, \tag{2.9b}$$

where β is a measure of the background density gradients and $k_{\rm D}^2 \doteq k^2 + 1$. Also, $S_{\rm ext}(t,y,\mathbf{k})$ in Eq. (2.7) is a source term for the fluctuations. The last term in Eq. (2.7) is the newly found collision operator for inhomogeneous DW turbulence. It is given by

$$C[J,J](t,y,\mathbf{k}) \doteq S_{\rm nl}[J,J] - 2\gamma_{\rm nl}[J]J, \tag{2.10}$$

where $\gamma_{\rm nl}[J]$ and $S_{\rm nl}[J,J]$ are

$$\gamma_{\rm nl}[J](t,y,\mathbf{k}) \doteq \int \frac{{\rm d}^2\mathbf{p}\,{\rm d}^2\mathbf{q}}{(2\pi\epsilon)^2}\, \delta^2(\mathbf{k}-\mathbf{p}-\mathbf{q})\, \Theta(t,y,\mathbf{k},\mathbf{p},\mathbf{q})\, M(\mathbf{p},\mathbf{q}) M(\mathbf{p},\mathbf{k})\, J(t,y,\mathbf{p}), \tag{2.11}$$

$$S_{\rm nl}[J,J](t,y,\mathbf{k}) \doteq \int \frac{{\rm d}^2\mathbf{p}\,{\rm d}^2\mathbf{q}}{(2\pi\epsilon)^2}\, \delta^2(\mathbf{k}-\mathbf{p}-\mathbf{q})\, \Theta(t,y,\mathbf{k},\mathbf{p},\mathbf{q})\, |M(\mathbf{p},\mathbf{q})|^2\, J(t,y,\mathbf{p}) J(t,y,\mathbf{q}). \tag{2.12}$$

Here $\Theta(t,y,\mathbf{k},\mathbf{p},\mathbf{q}) \doteq \pi\delta(\Delta\Omega)$, and

$$\Delta\Omega(t,y,\mathbf{k},\mathbf{p},\mathbf{q}) \doteq \Omega(t,y,\mathbf{k}) - \Omega(t,y,\mathbf{p}) - \Omega(t,y,\mathbf{q}). \tag{2.13}$$

One can identify $\Delta\Omega = 0$ as the frequency-resonance condition. Finally, the kernel $M(\mathbf{p},\mathbf{q})$ in Eqs. (2.11) and (2.12) is

$$M(\mathbf{p},\mathbf{q}) \doteq \mathbf{e}_z \cdot (\mathbf{p}\times\mathbf{q}) \left(q_{\rm D}^{-2} - p_{\rm D}^{-2}\right). \tag{2.14}$$

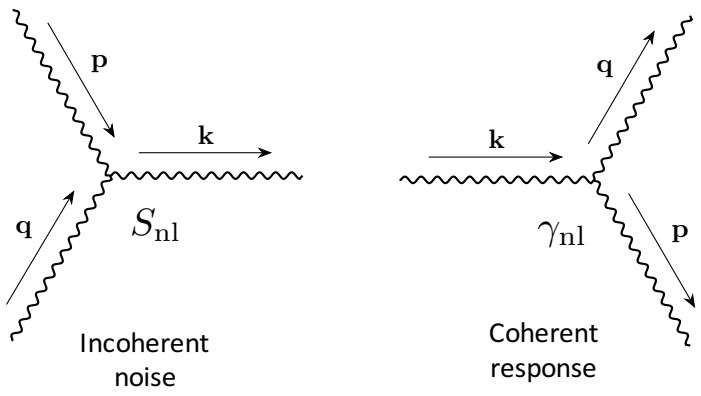

Figure 2-4. Schematic diagram of the nonlinear processes involved in the DW collision operator. The incoherent-noise term S_{nl} represents two DW quanta merging to produce a third DW fluctuation. The coherent response γ_{nl} is the opposite process, where one DW fluctuation decays into two other quanta.

Equations (2.7)–(2.14) are the main result of the work. These equations describe the coupled interaction between an *incoherent* wave bath of DWs and a *coherent* ZF velocity field. The collisional WKE (2.7) governs the dynamics of the wave-action density J for DWs. The left-hand side of Eq. (2.7) describes the wave refraction governed by the wave frequency Ω [Eq. (2.9a)], which serves as a Hamiltonian for the system. On the right-hand side, μ_{dw} represents weak dissipation due to the external environment, and Γ denotes linear dissipation caused by the ZFs [29; 24]. The term S_{ext} represents an external source term for the DW fluctuations.

The nonlinear term $C[J, J]$ in Eq. (2.7) plays the role of the wave scattering operator. It is composed of two terms, γ_{nl} and S_{nl}, which arise from nonlinear wave–wave interactions. The nonlinear source term S_{nl} in (2.12) is a bilinear functional on the action density J. It is always positive and represents contributions to $J(t, y, \mathbf{k})$ coming from waves with wavevectors $\mathbf{p}$ and $\mathbf{q}$ different from $\mathbf{k}$. This term is also known as (the variance of) *incoherent noise* [15]. The nonlinear damping-rate term γ_{nl} in Eq. (2.11) linearly depends on J and represents a sink term where the wave action in the $\mathbf{k}$ wavevector is transferred to other modes with different wavevectors. The effects described by γ_{nl} are called the *coherent response* [15]. These nonlinear wave–wave interactions are schematically represented in Fig. 2-4.

Equation (2.8) governs the dynamics of the ZFs. The second term on the left-hand side represents linear dissipation or drag acting on the ZF velocity field. The right-hand side acts as a source term for the generation of ZFs. Its origin can be traced back to Reynolds-stress term in the momentum equation for fluids. As shown, the source term for ZFs depends on a weighted integral over momentum of the DW distribution function.

The obtained formulation is fundamentally different from the previously reported homogeneous weak-wave-turbulence models for DW turbulence [11; 15]. While DWs are described as an incoherent fluctuating field as usual, ZFs are now treated as coherent structures, which are missed in homogeneous-turbulence theory. The obtained model motivates future investi-

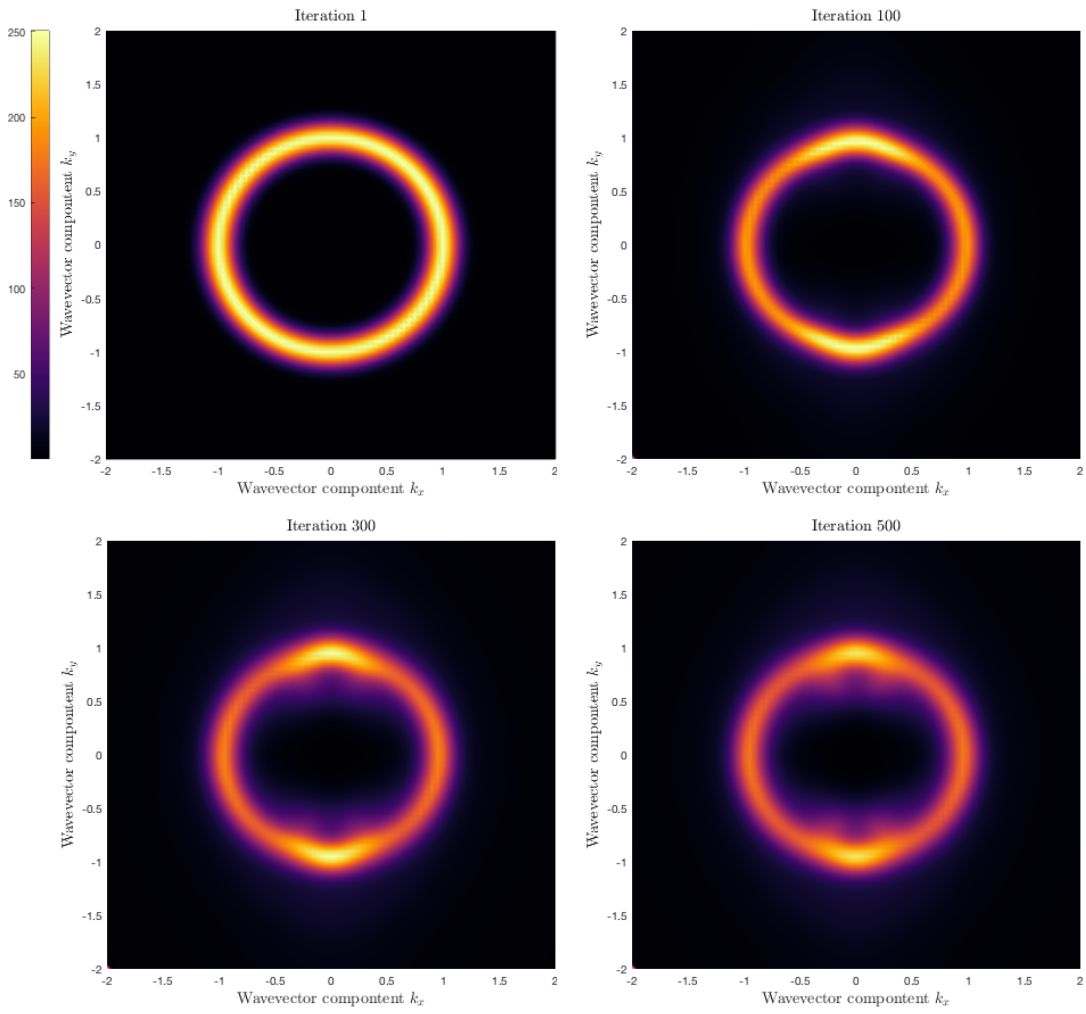

Figure 2-5. Sequence of images showing the convergence to the solution of the steady-state, homogenous collisional WKE given in Eq. (2.15).

gations of the effects of nonlinear wave–wave scattering on DW–ZF interactions, in particular, the spontaneous emergence of ZFs and the eventual saturation of the ZFs and the DW spectra. This theory might also help better understand the validity domain of the quasilinear approach to DW turbulence that has been commonly used in the literature.

2.3. Student-intern mentoring and numerical simulation of the obtained model

Reference [1] only presented the mathematical derivation for the collisional wave-kinetic-equation model. As part of Sandia's student-intern program, I worked with Daniel Davis to discretize the equations above and solve them numerically. Daniel Davis coded the equations above into a MatLab script. His work was financially supported by the research budget included in the Truman Fellowship.

It is important to mention that this internship was a great learning experience for Daniel Davis and myself. Working with Daniel Davis was a great opportunity to practice my mentoring skills. Before this project, Daniel had no prior experience on numerical integration of dynamical systems. During the first month of his internship, Daniel quickly learned how to discretize in both time and space some well-known linear PDEs, for example, the advection, the diffusion, and wave equations. In order to gain sufficient experience before tackling the main research project, Daniel and I reviewed these example problems, and he implemented the corresponding algorithms in `MATLAB`. For some problems, he solved the equations in both cartesian and cylindrical coordinates. He also implemented finite-difference and finite-volume schemes. I am happy to say that, at the end of his internship, Daniel implemented a finite-volume method that used a fifth-order variable–time-step Runge–Kutta integrator to solve the governing equations for drift waves and zonal flows. His code is the first algorithm that considers nonlinear wave–wave collisions in inhomogeneous turbulence.

To verify the collision operator implemented by Daniel, he implemented an iterative solver that would find the steady state solution of the homogeneous collisional wave-kinetic equation with no zonal flows:

$$0 = -\mu_{\mathrm{dw}} J + S_{\mathrm{ext}} + C[J, J]. \tag{2.15}$$

For this exercise, $S_{\mathrm{ext}}(\mathbf{k})$ was an annular-type forcing in momentum space. More specifically, $S_{\mathrm{ext}}(\mathbf{k}) \propto \exp\big(-(|\mathbf{k}|^2 - 1)/(2\sigma^2)\big)$. This type of forcing is typically used in DW calculations as it physically represents a DW source term that is isotropic in momentum space and that introduces fluctuation quanta at the scale of the ion gyroradius (in normalized units). Figure 2-5 shows several snapshots of the iterations in the steady-state solver. The initial guess was such that $J = S_{\mathrm{ext}}/\mu_{\mathrm{dw}}$. As shown, in the presence of the collision operator, the steady-state DW distribution function $W_{\mathrm{st}}(\mathbf{k})$ concentrates near the $(k_x, k_y) \simeq (0, \pm 1)$ regions. Interesting structures appear in the inner part of those regions as well. Since the shape of the DW distribution function is modified by the presence of the wave–wave collision operator, the growth rate of the ZFs in an inhomogeneous-turbulence simulation could be modified. This can be clearly seen from the source term on the right-hand side of Eq. (2.8). As shown, the forcing depends on the momentum integral of $k_x k_y W$. When calculating the integral, the isotropic annulus would lead to a larger value compared to the steady-state distribution function shown in Fig. 2-5. This simple exercise hints that perhaps DW collisions could slow down the ZF growth.

Figure 2-6 shows the time evolution of the ZFs with and without the effects of the nonlinear wave–wave collisions. As initial conditions for these simulations, the distribution function of the DWs was set to zero, and the ZF velocity was set to some random, small-amplitude noise. An isotropic, external source was added similar to that used above. The left-hand side of Fig. 2-6 shows the simulation result with no DW collisions. As shown, a coherent and periodic ZF appears spontaneously after some time. This is the so-called zonostrophic instability [19; 20; 21; 22; 23]. The code produced by Daniel agreed with the results given in previous works that did not include the effects of wave–wave collisions, e.g., see Refs. [28; 24; 29].

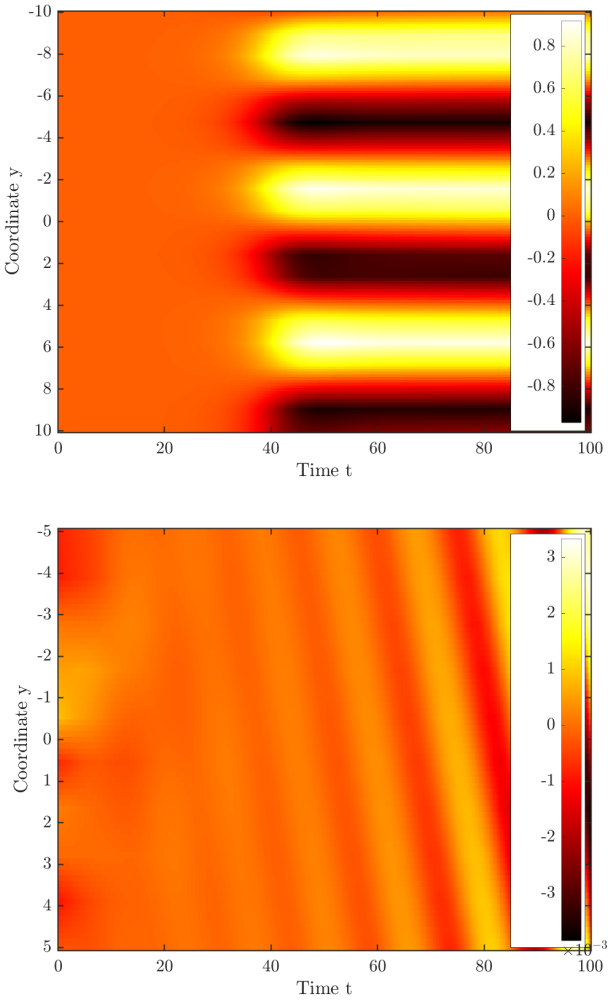

Figure 2-6. Time evolution of the ZF velocity. The top and bottom subfigures show simulation results including and not including nonlinear DW collisions, respectively. Simulation parameters were $\beta = 3$, $\mu_{\mathrm{dw}} = 0.25$, and $\mu_{\mathrm{zf}} = 0.1$.

The right-hand side of Fig. 2-6 shows the simulation result when including DW collisions. As shown, the change is quite dramatic: no ZFs appear. For this particular set of simulation parameters, the end state corresponds to an almost homogeneous, turbulent state. Therefore, it seems that the DW wave–wave collisions can effectively suppress the generation of ZFs. From these results, we believe that DW wave–wave collisions could play a role in the generation of ZFs. However, the examples shown in Fig. 2-6 were chosen to highlight the role that the DW collision operator can play. For other simulation parameters, ZFs would emerge regardless whether or not the collision operator was included. For this reason, a more detailed analysis needs to be done on these results, so no publication has yet come out from this work.

2.4. Conclusions and future work

As shown in the previous section, preliminary simulations show that DW collisions could play a role in the emergence of ZFs. However, some additional amount of work is needed to clear all the details and submit this result for publication.

As a more general comment, it is clear that phase-space methods provide an intuitive framework for the study of more general turbulence beyond that of DWs. Recently, these methods have been applied to study the emergence of large-scale structures from compressible Navier–Stokes turbulence [48]. Phase-space methods can also be useful for studying magneto-hydrodynamic (MHD) turbulence and the spontaneous emergence of large-scale magnetic fields (dynamo effect). For example, the magnetorotational dynamo has only been studied statistically using CE2 theory [49]. It would be interesting to investigate if a wave-kinetic description of the same problem can provide a simple intuitive model in which the interaction coefficients are explicitly given and where the growth rates can be computed analytically. Pursuing this line of research could open synergistic opportunities with university collaborators and enhance our understanding of the MHD turbulence in general.

3. VARIATIONAL WKB IN THE EULERIAN FRAME

3.1. Introduction

Nonlinear WKB is a powerful tool for studying solutions of partial differential equations (PDEs) in which there exists an explicit temporal and/or spatial scale separation. In these situations, the local behavior of solutions can be well approximated by a plane wave at any point. Nonlinear WKB, which is a generalization of the usual WKB method for linear PDEs, goes back at least to the mid 1960's, when it was used to study large-amplitude locally-plane-wave solutions of a variety of systems, including the Bousinesque equations [50] and the Kortweg-DeVries equation [51]. Generally speaking, given a (possibly nonlinear) system of PDEs of the form

$$F^b\big(\varphi^a(x), \partial_\mu \varphi^a(x), \dots\big) = 0, \tag{3.1}$$

where the unknown is multi-component field $\varphi^a(x)$, application of nonlinear WKB comprises two steps. First, Eq. (3.1) is extended to a larger system of PDEs using a procedure referred as "nonlinear WKB extension." Second, scale separation present in the original system of PDEs, either in F^b or the initial conditions, is leveraged to identify slow solutions of the extended system. As an example, this amounts to finding eigenmodes of wave equations. The power of this procedure comes from the fact that rapidly oscillating locally-plane-wave solutions φ^a of Eq. (3.1) correspond to slowly-varying solutions of the extended system, which are easier to treat using asymptotic methods.

In broad strokes, the nonlinear WKB extension procedure amounts to the following. First, one introduces the nonlinear WKB ansatz

$$\varphi^a(x) = \tilde{\varphi}^a\big(x, S(x)\big), \tag{3.2}$$

where $\tilde{\varphi}^a(x, \theta)$ is 2π-periodic in the second argument and $S(x)$ represents a phase function. More explicitly, since $\tilde{\varphi}^a$ is periodic in the second argument, it can be written as a sum of Fourier harmonics in θ so that

$$\tilde{\varphi}^a(x, \theta) = \sum_{n=-\infty}^{\infty} \hat{\varphi}^a_n e^{in\theta}. \tag{3.3}$$

Thus, the nonlinear WKB ansatz (3.2) differs from the conventional WKB ansatz in that it contains all harmonics in S. The term "nonlinear" is appropriate here because the ansatz (3.2) can handle nonlinear terms appearing in the PDE (3.1) that produce harmonic coupling. The ansatz (3.2) is then substituted into Eq. (3.1) and the chain rule is applied to express x-derivatives of φ in terms of x- and θ-derivatives of $\tilde{\varphi}$ and S. Finally, the argument $S(x)$

in any of the derivatives of $\tilde{\varphi}^a$ is replaced with any arbitrary angle θ in order to obtain the extended system:

$$F^b\big(\tilde{\varphi}^a(x,\theta), \partial_\mu \tilde{\varphi}^a(x,\theta) + \partial_\mu S(x) \partial_\theta \tilde{\varphi}^a(x,\theta), \dots\big) = 0. \tag{3.4}$$

The dependent variables are now $\tilde{\varphi}^a(x,\theta)$ and $S(x)$, while the independent variables are x and θ. Each solution $(\tilde{\varphi}^a, S)$ of Eq. (3.4) yields a solution φ^a of Eq. (3.1), with φ^a given by Eq. (3.2). In this sense, Eq. (3.4) extends the original equation (3.1).

In this work, we studied the nonlinear WKB extension procedure, i.e., the passage from Eq. (3.1) to Eq. (3.4), and its application to conventional field theories whose action functionals are assumed to be known. Specifically, we were concerned on how the nonlinear WKB extension can be applied to a particular class of PDEs from fluid mechanics known as Euler-Poincaré equations [52]. Such equations describe the evolution of ideal, i.e. dissipation-free, fluids. In the Euler-Poincaré setting, we addressed the question of whether structural properties of the original system of PDEs (3.1) are inherited by the extended equations (3.4).

3.2. Main result #1: Nonlinear WKB-extension of classical field theories

In the first part of Ref. [2], we showed how to obtain the NL-WKB extension of an arbitrary classical field theory, whose original action is assumed to be already known. In order to broadly present the main result, let us introduce the following basic concepts. Let φ be a multicomponent field defined on the manifold M. Within the compact subset $U \subset M$, the local action functional for φ is defined as

$$A_U(\varphi) = \int_U \mathcal{L}(x, \varphi(x), \partial\varphi(x))\, \mathrm{d}x. \tag{3.5}$$

Here $\partial\varphi(x)$ is a matrix that has entries $[\partial\varphi(x)]^a_\mu = \partial_\mu \varphi^a(x)$. We say that a field φ is a critical point of A_U if

$$\frac{d}{d\epsilon}\bigg|_0 A_U(\varphi + \epsilon\delta\varphi) = 0 \tag{3.6}$$

for all $\delta\varphi \in \mathcal{C}$ that vanish on the boundary ∂U of the subset U.

Suppose that $\mathcal{C}$ contains all smooth fields with compact support. Then it is a standard result in the calculus of variations that φ is a critical point of A_U for all $U \subset M$ if and only if φ satisfies the system of second-order PDE known as the Euler-Lagrange equations:

$$\frac{\partial \mathcal{L}}{\partial \varphi^a}(x, \varphi(x), \partial\varphi(x)) = \frac{\partial}{\partial x^\mu}\left(\frac{\partial \mathcal{L}}{\partial v^a_\mu}(x, \varphi(x), \partial\varphi(x))\right), \tag{3.7}$$

where $v^a_\mu(x) \doteq \partial_\mu \varphi^a$. This kind of systems is referred as a first-order classical field theory.

Given a first-order classical field theory, the NL-WKB extension procedure may be applied to the theory's Euler-Lagrange equations. From the discussion given in the Introduction

of this Chapter, the NL-WKB extension of the Euler–Lagrange equations (3.7) is the system of partial differential equations

$$\frac{\partial \mathcal{L}}{\partial \varphi^a}(j(x,\theta)) = \left(\frac{\partial}{\partial x^\mu} + \partial_\mu S(x)\frac{\partial}{\partial \theta}\right)\left(\frac{\partial \mathcal{L}}{\partial v^a_\mu}(j(x,\theta))\right), \tag{3.8}$$

where

$$j(x,\theta) = \big(x, \tilde{\varphi}(x,\theta), \partial\tilde{\varphi}(x,\theta) + \partial_\theta\tilde{\varphi}(x,\theta)\partial S(x)\big) \tag{3.9}$$

is convenient shorthand notation. In the above, $\tilde{\varphi} = \tilde{\varphi}(x,\theta)$ is the extended field that depends on the coordinate x of the manifold M and on the coordinate θ for the local phase. Here $S = S(x)$ is a phase function that depends on x. As discussed in the previous section, the parameter θ is arbitrary and acts as an additional coordinate.

In Ref. [2], the first goal was to determine whether an action functional that directly generates Eq. (3.8) exists, and if so, how can we find its expression. It is worth mentioning that the reason why this is an important question to be answered is that, once a convenient action principle is identified, it can then be used to discover underlying properties of the scale-separated system. This occurs because all the information about the physical system is contained with the Lagrangian. Also, asymptotic models can be derived by approximating the Lagrangian only. Conservation properties of the original and reduced system can be deduced by identifying symmetries of their corresponding Lagrangians. In summary, directly working with the Lagrangian allows to perform well-controlled approximations of the original physical system.

Excitingly, the corresponding NL-WKB action for Eq. (3.8) does exist, and we developed a systematic approach to find it in Ref. [2]. In this report, I shall only provide some heuristic arguments that hint to the result. Suppose φ is a solution of the Euler-Lagrange equations that locally has the appearance of a plane wave. Formally, we write $\varphi(x) = \tilde{\varphi}(x, S(x))$. By the chain rule, these functions satisfy

$$\frac{\partial \mathcal{L}}{\partial \varphi^a}(j(x,\theta))\bigg|_{\theta=S(x)} = \frac{\partial}{\partial x^\mu}\left(\frac{\partial \mathcal{L}}{\partial v^a_\mu}(j(x,S(x)))\right) = \left(\frac{\partial}{\partial x^\mu} + \partial_\mu S(x)\frac{\partial}{\partial \theta}\right)\left(\frac{\partial \mathcal{L}}{\partial v^a_\mu}(j(x,\theta))\right)\bigg|_{\theta=S(x)}, \tag{3.10}$$

where we have used the shorthand notation $j(x,\theta)$ introduced in Eq. (3.9). Because the phase function is rapidly rotating, we can extract more information from Eq. (3.10) by considering the latter in a spacetime region that is small compared with the long spacetime scale, but large compared with the short spacetime scale. In other words, this can be considered as a mesoscale region. In such a region, we may regard the argument x in $j(x, S(x))$ as being fixed, while the argument $S(x)$ retains its rapidly oscillating character. If we make the assumption that $S(x)$ makes at least one complete rotation in our intermediate, mesoscale region, we may therefore conclude that Eq. (3.8), which is the strengthened version of Eq. (3.10), must be satisfied.

Now, let us consider the application of similar heuristic arguments to the original variational principle whose action is given by Eq. (3.5). Suppose once more that φ is a solution of

the field theory that is locally a plane wave. Then, as before, we may write $\varphi(x) = \tilde{\varphi}(x, S(x))$. Moreover, the action A_U evaluated on this special φ can be written as

$$A_U(\varphi) = \int_U \mathcal{L}(j(x, S(x)))\,\mathrm{d}x. \tag{3.11}$$

Because the phase function S is rapidly oscillating by hypothesis, we may partition the integration domain $U = \cup_i U_i$ into cells with diameters that are large compared with the short scale and short compared with the large scale, and then write $A_U(\varphi) = \sum_i A_{U_i}(\varphi)$. In each of the integrals A_{U_i} the first argument of $j(x, S(x))$ may be replaced with the center x_i of cell U_i without appreciably changing the value of the integral. Moreover, because $S(x)$ varies rapidly in U_i, the dominant contribution to the integral A_{U_i} is given by averaging over $S(x)$ according to

$$A_{U_i} \approx \frac{1}{2\pi} \int_0^{2\pi} \int_{U_i} \mathcal{L}(j(x_i, \theta))\,\mathrm{d}x\,\mathrm{d}\theta. \tag{3.12}$$

If we now interpret the previously established formula $A_U(\varphi) = \sum_i A_{U_i}(\varphi)$ as a Riemann sum, we conclude that the action functional evaluated on a locally-plane φ is approximately

$$\begin{aligned} A_U(\varphi) &\approx \frac{1}{2\pi} \int_0^{2\pi} \int_U \mathcal{L}(j(x, \theta))\,\mathrm{d}x\,\mathrm{d}\theta \\ &\equiv \tilde{A}_{U\times S^1}(\tilde{\varphi}, S), \end{aligned} \tag{3.13}$$

where we have introduced the extended action functional $\tilde{A}_{U\times S^1}(\tilde{\varphi}, S)$. Here S^1 denotes the interval $[0, 2\pi)$. Moreover, because φ is by assumption a critical point of A_U, this argument suggests that

$$\left.\frac{\mathrm{d}}{\mathrm{d}\epsilon}\right|_0 \tilde{A}_{U\times S^1}(\tilde{\varphi} + \epsilon\delta\tilde{\varphi}, S + \epsilon\delta S) \approx 0, \tag{3.14}$$

where $\delta\tilde{\varphi}(x, \theta)$ and $\delta S(x)$ are arbitrary functions that vanish when $x \in \partial U$. These heuristic arguments hint that Eq. (3.8) do follow from a variational principle.

In Ref. [2], it is shown that the action principle that generates Eq. (3.8) is indeed given by Eq. (3.13), or more explicitly,

$$A_{U\times S^1}(\tilde{\varphi}, S) = \frac{1}{2\pi} \int_{S^1} \int_U \mathcal{L}(x, \tilde{\varphi}(x, \theta), \partial\tilde{\varphi}(x, \theta) + \partial_\theta\tilde{\varphi}(x, \theta)\partial S(x))\,\mathrm{d}x\,\mathrm{d}\theta. \tag{3.15}$$

The action above is a functional over the fields $\tilde{\varphi}$ and the phase function S. Note that the action functional above is identical to Whitham's averaged Lagrangian [53; 54]. When varying the action with respect to the fields $\tilde{\varphi}$ and S, we obtain

$$\frac{\partial\mathcal{L}}{\partial\tilde{\varphi}^a} = \left(\frac{\partial}{\partial x^\mu} + \partial_\mu S\frac{\partial}{\partial\theta}\right)\left(\frac{\partial\mathcal{L}}{\partial\tilde{v}^a_\mu}\right), \tag{3.16}$$

$$0 = \frac{\partial}{\partial x^\mu} \int_{S_1} \frac{\partial\tilde{\varphi}}{\partial\theta}\frac{\partial\mathcal{L}}{\partial\tilde{v}_\mu}\,\mathrm{d}\theta, \tag{3.17}$$

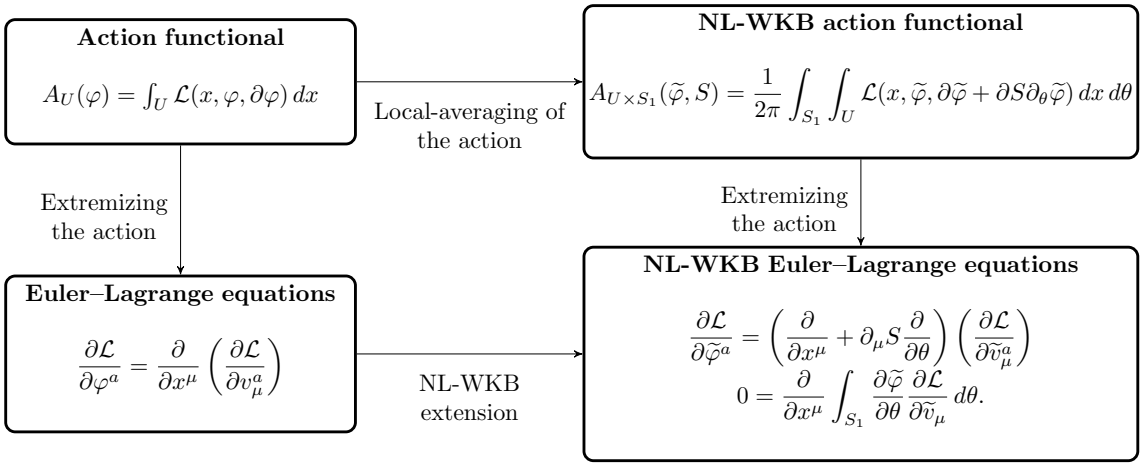

Figure 3-1. The nonlinear WKB extension of ordinary first-order classical field theories.

where I have omitted writing the explicit variable dependencies. Of course, the first equation (3.16) corresponds to the NL-WKB extension of the original Euler–Lagrange equation given in Eq. (3.8). This equation arises from the variation of the action with respect to $\tilde{\varphi}$. Equation (3.17) is obtained when varying the action with respect to S and is physically interpreted as an action-conservation equation. More fundamentally, this last equation arises from the gauge symmetry of the action with respect to constant rotations of the phase θ. The main ideas between the action principle, the Euler–Lagrange equations, and their corresponding NL-WKB extended versions are summarized in Fig. 3-1.

3.3. Main result #2: NL-WKB extension of Euler–Poincaré fluid systems

The result discussed above is useful for identifying variational principles that govern the NL-WKB extension of a large class of dissipation-free PDEs. However, it is not directly applicable to PDEs commonly used for modeling fluid dynamics. In particular, they cannot be applied directly to the fluid-mechanical PDEs that arise from Euler–Lagrange or Euler–Poincaré variational principles.

Let us consider the ideal isothermal Euler equations in order to understand the main difficulty when dealing with fluid equations. The isothermal Euler equations are given by

$$\partial_t\rho + \boldsymbol{\nabla}\cdot(\rho\mathbf{u}) = 0, \tag{3.18}$$

$$\rho(\partial_t\mathbf{u} + \mathbf{u}\cdot\boldsymbol{\nabla}\mathbf{u}) = -c^2\boldsymbol{\nabla}\rho \tag{3.19}$$

where the unknown fields are the mass density $\rho(t, \mathbf{x})$ and the fluid velocity $\mathbf{u}(t, \mathbf{x})$. Here c is a constant representing the speed of small-amplitude sound waves. This system of equations fits the general type of PDEs discussed in the previous section. Equations (3.18) and (3.19) arise from an Euler-Lagrange variational principle [52], which is explained as

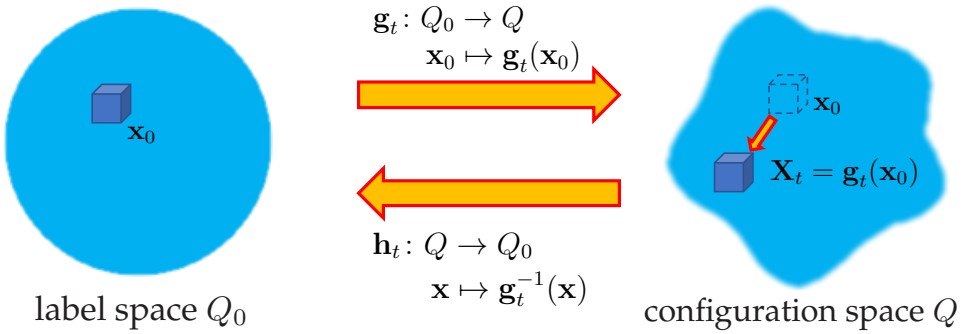

Figure 3-2. The configuration map $\mathbf{g}_t$ encodes the information on the temporal dynamics of the fluid elements with labels $\mathbf{x}_0$. Its inverse $\mathbf{h}_t \doteq \mathbf{g}_t^{-1}$ is called the back-to-labels map. The function $\mathbf{h}_t$ provides the label $\mathbf{x}_0$ of the fluid element found at an Eulerian position $\mathbf{x}$ at time t.

follows. Let Q be a compact region that represents the fluid container, and let Q_0 be a diffeomorphic copy of Q equipped with a non-vanishing function $\rho_0 : Q_0 \to \mathbb{R}$ that represents a reference configuration of fluid elements. A path $t \mapsto \mathbf{g}(t) \in \mathrm{Diff}(Q_0, Q)$ in the space of diffeomorphisms $Q_0 \to Q$ is a critical point of the functional

$$\mathcal{A}_{\rho_0}(\mathbf{g}) = \int_{t_1}^{t_2} \int_{Q_0} \frac{1}{2} |\dot{\mathbf{g}}(\mathbf{x}_0)|^2 \, \rho_0(\mathbf{x}_0) \, \mathrm{d}\mathbf{x}_0 - \int c^2 \rho_0(\mathbf{x}_0) \ln \left(\frac{\rho_0(\mathbf{x}_0)}{\det(\boldsymbol{\nabla}_0 \mathbf{g})(\mathbf{x}_0)} \right) \mathrm{d}\mathbf{x}_0 \tag{3.20}$$

if and only if Eq. (3.19) is satisfied with ρ and $\mathbf{u}$ defined according to

$$\rho(\mathbf{x}) = \frac{1}{\det(\boldsymbol{\nabla}_0 \mathbf{g})(\mathbf{g}^{-1}(\mathbf{x}))} \rho_0(\mathbf{g}^{-1}(\mathbf{x})), \tag{3.21}$$

$$\mathbf{u}(\mathbf{x}) = \dot{\mathbf{g}}(\mathbf{g}^{-1}(\mathbf{x})), \tag{3.22}$$

where we have suppressed the time argument t for the sake of presentation. In particular, because ρ is defined by Eq. (3.21), the continuity equation (3.18) is satisfied.

Before continuing further, it might be worth explaining the physical origin of the configuration map $\mathbf{g}_t$. Suppose that, at the initial time t_0 before the system is evolved, one divides the fluid into infinitesimally small elements. We then assign to each element a so-called label, which for convenience could be their initial positions $\mathbf{x}_0$. The configuration map $\mathbf{g}_t$ encodes the information about the temporal motion of these fluid elements. Specifically, for an element with label $\mathbf{x}_0$ it provides its position $\mathbf{X}_t$ at each time t. Similarly, the inverse function of $\mathbf{h}_t \doteq \mathbf{g}_t^{-1}$ is called the back-to-labels map. Physically, when providing an Eulerian position $\mathbf{x}$ and a time t, the back-to-labels map provides the label $\mathbf{x}_0$ of the fluid element found at that position. These notions are illustrated in Fig. 3-2.

The difficulty with Eq. (3.20) is that the field that appears in the action functional is $\mathbf{g}(\mathbf{x}_0, t)$ instead of $\rho(t, \mathbf{x})$ or $\mathbf{u}(t, \mathbf{x})$, as one might expect from experience with classical field theory. In fact, $\mathbf{g}$ is not even defined on the same *domain* as ρ or $\mathbf{u}$. (The domain of $\mathbf{g}_t$ is technically the label space Q_0.) It is not at all obvious how the NL-WKB extension procedure

can be applied to the variational principle of Eqs. (3.18) and (3.19). This occurs because it is not physical to assign a phase $S(x)$ to a field that lives in the configuration space Q_0; in other words, phases are assigned to Eulerian positions, not labels or initial positions.

To remedy this problem, we introduced a phase-space variational principle that does fit the mold of classical field theories. For the particular case of isothermal fluids, the Lagrangian of this variational principle is given by [2]

$$L = \int_Q (\rho \mathbf{u} \cdot \mathbf{v} + \rho(\partial_t + \mathbf{v} \cdot \boldsymbol{\nabla})\chi)\, \mathrm{d}^3\mathbf{x} - \int_Q \left[\frac{\rho}{2}\,|\mathbf{u}|^2 + c_s^2 \rho \,\ln\left(\frac{\rho}{\rho_{\mathrm{ref}}}\right)\right] \mathrm{d}^3\mathbf{x}, \tag{3.23}$$

where ρ is the fluid density, $\mathbf{u}$ is the fluid velocity, χ is a scalar field that acts as a Lagrange multiplier, and ρ_{ref} is a reference density. Note that the $\mathbf{v}(t, \mathbf{x})$ is an independent fluid velocity that is defined via the inverse of the configuration map, $\mathbf{h} \doteq \mathbf{g}^{-1}$, which is the back-to-labels map introduced earlier. In terms of the configuration map, the velocity field $\mathbf{v}$ is usually defined as $\mathbf{v} \doteq \dot{\mathbf{g}} \circ \mathbf{g}^{-1}$, or equivalently $\mathbf{v}(t, \mathbf{x}) = [\partial_t g(t, \mathbf{x}_0)]_{\mathbf{x}_0 = \mathbf{g}^{-1}(t,\mathbf{x})}$. In terms of the back-to-labels map, it is equivalently written as

$$\mathbf{v} \doteq -\dot{\mathbf{h}} \cdot (\boldsymbol{\nabla}\mathbf{h})^{-1}. \tag{3.24}$$

Note that, in contrast to the action given in Eq. (3.20), here the fields $\mathbf{h}$, ρ, $\mathbf{u}$, and χ are all independent. Therefore, this variational principle falls into the class of conventional field theories that was discussed in the previous section.

For the sake of clarity, let us take the variations of action with Lagrangian (3.23). We first note that the back-to-labels map $\mathbf{h}$ only appears in the Lagrangian through the velocity field $\mathbf{v}$. Therefore, it can be shown that, when varying the $\mathbf{h}$, this will induce a variation on $\mathbf{v}$ such that $\delta\mathbf{v} = \dot{\boldsymbol{\xi}} + (\mathbf{v} \cdot \boldsymbol{\nabla})\boldsymbol{\xi} - (\boldsymbol{\xi} \cdot \boldsymbol{\nabla})\mathbf{v}$, where $\boldsymbol{\xi} \doteq -\delta\mathbf{h} \cdot (\boldsymbol{\nabla}\mathbf{h})^{-1}$. In some sense, one could say that the variations of $\mathbf{v}$ are constrained. The resulting Euler–Lagrange equations are given by

$$\delta\mathbf{u}: \quad \mathbf{v} = \mathbf{u}, \tag{3.25}$$

$$\delta\chi: \quad \partial_t \rho + \boldsymbol{\nabla} \cdot (\rho \mathbf{v}) = 0, \tag{3.26}$$

$$\delta\rho: \quad \partial_t \chi + \mathbf{v} \cdot \boldsymbol{\nabla}\chi = -\mathbf{u} \cdot \mathbf{v} + \frac{1}{2}|\mathbf{u}|^2 + c_s^2 + c_s^2 \ln\left(\frac{\rho}{\rho_{\mathrm{ref}}}\right), \tag{3.27}$$

$$\delta\mathbf{h}: \quad \partial_t(\rho\mathbf{u} + \rho\boldsymbol{\nabla}\chi) + \boldsymbol{\nabla} \cdot [\mathbf{v} \otimes (\rho\mathbf{u} + \rho\boldsymbol{\nabla}\chi)] = -(\rho u_i + \rho\partial_i\chi)\boldsymbol{\nabla}v^i. \tag{3.28}$$

This system of equations comprises more equations than the original isothermal Euler equations (3.18) and (3.19). Nevertheless, the fields $\mathbf{v}$ and χ can be easily eliminated. Doing so immediately leads to the isothermal Euler equations that we wanted to derive.

The more general case of barotropic Euler equations was treated in Ref. [2]. This allowed us to cast this type of fluid equations into the framework of conventional classical field theories. After doing so, we then found a variational principle for the NL-WKB extended fluid equations. Another interesting theoretical result that was shown is that the variational principle for the extended WKB fluid system admits loops of relabeling transformations

as a symmetry group. Therefore, Noether's theorem implies that the NL-WKB extended Eulerian equations possess a family of circulation invariants parameterized by S^1.

As a pedagogical example of how the methods developed can be useful, we used the techniques above to obtained a reduced, asymptotic model describing wave–mean-flow interactions [2]. Specifically, we studied the time-averaged interaction between a small-amplitude, high-frequency acoustic wave and a slowly varying isothermal perfect fluid. The main steps of the calculation were the following. We first cast the variational principle for isothermal fluids in the WKB framework. Then, we separated the fields into a slowly-varying component representing the background fluid motion and a rapidly-varying component representing the small-amplitude acoustic wave. Using ideas from slow-manifold theory [55; 56], we solved for the rapidly-varying fields. (This was equivalent to finding the eigenmodes corresponding to acoustic oscillations.) Once the expressions for the rapidly-varying fields were obtained, these were inserted back into the NL-WKB extended Lagrangian. The Lagrangian was then simplified and truncated to the leading order in the amplitude of the acoustic wave.

The resulting action principle describing the wave–mean-flow interaction is given by $\overline{\mathsf{A}} = \int_{t_1}^{t_2} \overline{\mathsf{L}}\,\mathrm{d}t$, where the Lagrangian $\overline{\mathsf{L}}$ is

$$\begin{aligned}\overline{\mathsf{L}}(\bar{\mathbf{h}}, \bar{\mathbf{u}}, \bar{\rho}, \bar{\chi}, \mathcal{I}, S) = &\int_Q \left[\bar{\rho}\bar{\mathbf{u}}\cdot\bar{\mathbf{v}} + \bar{\rho}\big(\partial_t\bar{\chi} + \bar{\mathbf{v}}\cdot\boldsymbol{\nabla}\bar{\chi}\big)\right]\,\mathrm{d}^3\mathbf{x}\\ &- \int_Q \left[\frac{\bar{\rho}}{2}\,|\mathbf{u}|^2 + c_s^2\bar{\rho}\,\ln\left(\frac{\bar{\rho}}{\rho_{\mathrm{ref}}}\right)\right]\mathrm{d}^3\mathbf{x}\\ &- \epsilon^2\int_Q \mathcal{I}\,(\partial_t S + \bar{\mathbf{v}}\cdot\boldsymbol{\nabla}S + c_s|\boldsymbol{\nabla}S|)\,\mathrm{d}^3\mathbf{x}. \end{aligned} \tag{3.29}$$

In the Lagrangian above, the first line on the right-hand side represents the symplectic part of the action. Here the variables $\bar{\rho}$, $\bar{\mathbf{u}}$, and $\bar{\mathbf{v}} \doteq -\dot{\bar{\mathbf{h}}}\cdot(\boldsymbol{\nabla}\bar{\mathbf{h}})^{-1}$ represent the bulk flow variables. It is worth clarifying that the mean back-to-labels map $\bar{\mathbf{h}}$ and the mean configuration map $\bar{\mathbf{g}}$ describe the bulk fluid motion that is supposed to be slowly varying. Also, here $\bar{\chi}$ acts as a Lagrange multiplier that enforces the continuity equation. The second line in Eq. (3.29) represents the Hamiltonian for the bulk fluid flow. It is composed by a kinetic component and a potential component related to the fluid pressure. Finally, the last line corresponds to the Lagrangian describing the wave motion. Here S is the phase function for the acoustic oscillation, and $\mathcal{I}$ is the acoustic-wave action density, which is given by

$$\mathcal{I} \doteq \frac{1}{2\pi}\int_{S^1}\bar{\rho}\,\frac{c_s}{|\boldsymbol{\nabla}S|}\left(\frac{\tilde{\rho}}{\bar{\rho}}\right)^2\mathrm{d}\theta, \tag{3.30}$$

where $\tilde{\rho}(t, \mathbf{x}, \theta)$ is the fluctuating density.

In the wave–mean-flow action with Lagrangian (3.29), the independent fields are $\bar{\mathbf{h}}$, $\bar{\rho}$, $\bar{\mathbf{u}}$, $\bar{\chi}$, $\mathcal{I}$, and S. Varying the action with respect to these fields and eliminating the fields $\bar{\mathbf{v}}$

and $\bar{\chi}$ leads to the following governing equations:

$$\partial_t \bar{\rho} + \boldsymbol{\nabla} \cdot (\bar{\rho} \bar{\mathbf{u}}) = 0, \tag{3.31}$$

$$\bar{\rho} \partial_t \bar{\mathbf{u}} + \bar{\rho} \bar{\mathbf{u}} \cdot \boldsymbol{\nabla} \bar{\mathbf{u}} = -c_s^2 \boldsymbol{\nabla} \bar{\rho} - \boldsymbol{\nabla} \left(\mathcal{I} \frac{\boldsymbol{\nabla} S \otimes \boldsymbol{\nabla} S}{|\boldsymbol{\nabla} S|} \right), \tag{3.32}$$

$$\partial_t \mathcal{I} + \boldsymbol{\nabla} \cdot (\mathbf{v}_g \mathcal{I}) = 0, \tag{3.33}$$

$$\partial_t S + \bar{\mathbf{u}} \cdot \boldsymbol{\nabla} S + c_s |\boldsymbol{\nabla} S| = 0. \tag{3.34}$$

These equations describe a high-frequency, small-amplitude acoustic wave interacting with a slowly-varying, isothermal bulk fluid. Equation (3.31) is obviously the continuity equation for the bulk flow. Equation (3.32) corresponds to the momentum conservation equation. Note that the last term represents a ponderomotive pressure acting on the bulk fluid which is generated by the acoustic wave. Equation Eq. (3.33) represents the action conservation equation for the acoustic wave. In essence, this equation propagates the envelope of the acoustic wave. Finally, Eq. (3.34) represents the dispersion relation. In this case, $\omega(t, \mathbf{x}) \doteq -\partial_t S$ is the wave frequency, $\mathbf{k}(t, \mathbf{x}) \doteq \boldsymbol{\nabla} S$ is the wavevector, and $\Omega(t, \mathbf{x}) \doteq \bar{\mathbf{u}} \cdot \mathbf{k} + c_s |\boldsymbol{\nabla} S|$ is the Doppler-shifted acoustic-wave frequency.

3.4. Conclusions and future work

The principle objective of the original proposal that was submitted for the Truman Fellowship was to develop an advanced theoretical model for laser–plasma interactions (LPI) in magnetized environments such as those encounted in the MagLIF preheat stage [57; 58]. It was initially thought that the techniques that were being developed in this work would eventually serve as a building block for tackling the much harder LPI problem. However, towards the end of this project, it was concluded that these techniques were not going to be useful to describe in detail the MagLIF preheat stage and that the cost-benefit ratio for continuing such a project would be too high. In other words, results coming from the originally proposed project would not impact much the mainstream research done at Sandia. Below, I shall expand more on these ideas and briefly mention some of the major setbacks that were encountered.

Starting with the technical aspects, one of the first difficulties that emerged was that the technique of slow-manifold reduction was mathematically "too rigid" for systematically deriving the sought LPI model. As an example, when introducing the scale separation for the eventual asymptotic analysis, the mathematics would force the frequency of the electromagnetic waves to be much higher than the plasma frequency. This would physically cause the electromagnetic waves to not refract at all by the surrounding plasma. Without the possibility of refraction, there was no chance that the electromagnetic waves would self-focus, which is an effect that is often seen in preheat experiments. It is possible, however, that this difficulty could have been overcome with additional work.

The MagLIF preheat environment is also uniquely challenging to model using a classical field theory. Inverse Bremsstrahlung is the main mechanism for heating the plasma when the

laser is injected into the MagLIF fuel. This mechanism is caused by collisions of oscillating electrons with the surrounding plasma ions. Describing this process within the framework of a variational principle is not straightforward, as it is essentially a dissipative process that removes laser quanta (or wave action) and transfers the laser energy to the plasma. Another technical difficulty was that, in the typical laser intensity in which the Z beamlet laser operates for laser preheating, the filamentation of the laser is thermally driven rather than ponderomotively driven. As the name suggests, ponderomotive filamentation is driven by conventional ponderomotive forces and is the dominant effect in high-intensity lasers. These forces can be readily described by variational principles [59; 60; 61; 62]. In contrast, thermal filamentation involves the effects of heat conduction [63] and is usually dominant for lower-intensity lasers. Modeling heat conduction is notoriously more difficult within a variational framework. Both absorption by inverse Bremsstrahlung and thermal filamentation modify the laser intensity profile, which in turn modifies the processes in LPI such as stimulated scattering.

From a more practical standpoint, there were also other concerns on how a new developed LPI model would actually be implemented into a production code currently used at Sandia. The main production codes that are currently used for describing experiments on Z are based on the magneto-hydrodynamic (MHD) approximation. Within this approximation, the codes can impressively describe many aspects of the experiments done on Z. However, by the nature of the approximation itself, the codes are incapable of describing electrostatic oscillations. As it is well known, it is necessary to capture these oscillation since they are necessary to describe stimulated Raman scattering. Without the computational capability to self-consistently model these oscillations or to implement a sufficient model for them into a production code in a timely manner, it quickly became dubious if any model that would arise from this research could actually be put into practical use.

Having said the above, the theoretical tools that were developed in this project could be used to describe more complex academic scenarios involving nonlinear waves interacting with bulk fluid flow. For example, expanding the Lagrangian to higher-order terms with respect to the wave amplitude should lead to effects such as wave harmonic generation and nonlinear couplings between multiple waves, e.g., stimulated scattering [64]. Other possibilities include studying corrections to ray trajectories caused by space-dependent wave polarization [65; 66; 67] in wave–mean-flow problems arising in fluids and plasmas.

As a final note, one of the advantages of the Truman Fellowship is that it provides the Fellow the freedom to explore the diverse research areas pursued at Sandia without the hesitation of immediately being forced to be involved in a research project. After learning more about the local research thrusts and discovering the difficulties that lied ahead for the originally proposed project, I decided that it was perhaps more beneficial to Sandia if I changed the focus of my research to topics that were more relevant to the local effort. In this vein and as it will be shown below, this shift in focus led to research projects on the magnetic Rayleigh–Taylor instability which affects confinement in MagLIF experiments and on the scaling of magneto-inertial fusion targets to larger pulsed-power drivers.

4. WEAKLY NONLINEAR MAGNETIC RAYLEIGH–TAYLOR INSTABILITY

4.1. Introduction

The magnetic-Rayleigh–Taylor instability (MRTI) occurs in pinch plasmas in which the $\mathbf{J} \times \mathbf{B}$, or magnetomotive, force is used to compress matter [68; 69; 70; 71]. For example, in the MagLIF experimental platform [72; 73; 74; 75], the MRTI develops as the driving magnetic pressure accelerates the liner throughout the implosion. In analogy to the classical Rayleigh–Taylor instability, this configuration is dynamically unstable. In general, it is important to better understand MRTI since it can compromise the integrity of metal liners, which in turn, is a significant factor for determining target performance in MagLIF [76].

The magnetic-Rayleigh–Taylor (MRT) instability has been extensively studied throughout the years. Refs. [77; 78] reported the use of radiograph-based techniques to diagnose the dynamics of seeded MRT instabilities on Z-pinch implosions. Shortly afterwards, MRT growth was experimentally characterized on smooth coated and uncoated liners [79; 80]. In Ref. [81], the spontaneous appearance of helical structures in axially magnetized Z pinches was reported. These structures were also investigated in further detail in Refs. [82; 83]. Finally, MRTI was also experimentally studied in planar geometry in Ref. [84].

From the theoretical perspective, the first studies on MRTI were done by Kruskal and Schwarzchild [85], Chandrasekhar [86], and Harris [87]. After those seminal works, linear MRTI was further investigated by including various additional effects. For example, Refs. [88; 89] discussed linear MRTI in a slab geometry while including magnetic fields embedded inside the conducting fluid. MRTI was also investigated in cylindrical geometry [90], and the analysis was extended to finite-width shells [91]. The stabilizing effects due to finite compressibility and elasticity of the heavy conducting fluid were reported in Refs. [92; 93; 94; 95]. Similarly, sheared flows and sheared magnetic fields were found to be MRT stabilizing in Refs. [96; 97]. The effects due to axial magnetic-flux compression on the liner exterior were investigated in Ref. [98] to explain the helical structures reported in Ref. [81]. Finally, Bell–Plesset effects in imploding shells were discussed in Refs. [99; 100], and the effects due to finite-Larmor radius were also investigated in Ref. [101].

The theoretical studies above have primarily investigated MRTI in the linear phase. However, it is well known that MRT perturbations can develop strong nonlinear structures during current-driven implosions [79; 80; 81]. In this regard, numerical simulations have been used to study nonlinear MRTI in Z-pinch implosions. As an example, the effects of MRTI on the integrity of imploding cylindrical liners were studied in Refs. [102; 103]. The emergence of helical structures in axially magnetized Z pinches was also investigated

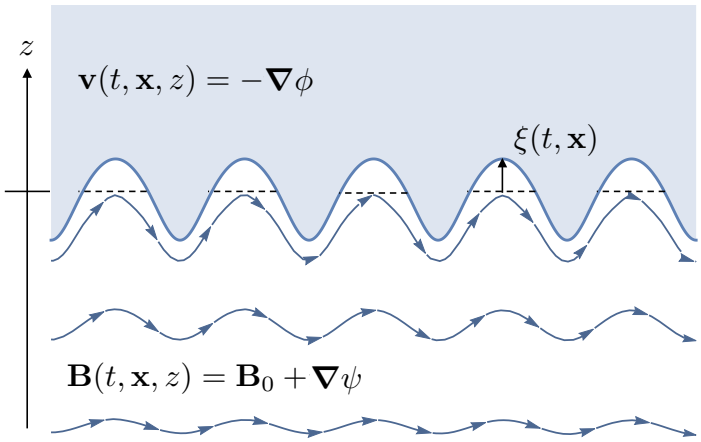

Figure 4-1. Schematic diagram of the geometry considered for the present MRTI study. The fluid slab is denoted by the shaded region. The magnetic field is represented by the stream lines. The field $\xi(t,\mathbf{x})$ describes the fluid–vacuum interface.

numerically [104]. From the theoretical perspective, interesting results on nonlinear RTI and MRTI in accelerating planar slabs and cylindrical implosions have been reported [105; 106; 107; 108; 109]. Concerning MRTI in cylindrical implosions [106; 107; 108; 109], these studies used the so-called thin-shell approximation where the wavelength of the perturbations is large compared to the shell thickness. Although this approximation only covers a subset of possible MRTI modes, it does allow to analytically investigate the fully nonlinear stages of this instability with relatively simple mathematical methods.

Given the fundamental importance of this instability for Z-pinch implosions, as part of the Truman Fellowship, I studied the weakly-nonlinear stage of the MRTI. To simplify the analysis of the problem, I considered the single-interface MRT problem considered in Refs. [85; 86]. A schematic of the geometry considered is shown in Fig. 4-1. In this problem, a semi-infinite fluid slab is supported by a magnetic field. Here the magnetic field plays the role of a light fluid supporting the heavy fluid on top. The goal of this study was to develop a theoretical model that allowed for the generation of MRT harmonics and for their eventual coupling. Such a model was developed using the framework of variational principles. The model described the emergence of MRT spikes and bubbles, and it was also used to calculate the effects of the magnetic field on the saturation amplitude of the MRTI exponential growth. I shall briefly discuss some details of these results below. Results from this work were published in Ref. [3].

4.2. Main result #1: Development of a MRTI variational principle

One way to construct well-controlled asymptotic approximations for dynamical systems is to directly approximate a variational principle $\delta\Lambda = 0$ from which the exact equations can be derived [110; 111; 66; 61]. Based on a variational principle for irrotational fluids with a

free surface [112], I found that the action Λ for the MRTI can be written as

$$\Lambda = \int_{t_1}^{t_2} L[\xi, \phi, \psi, \partial_t \xi, \partial_t \phi] \, \mathrm{d}t, \tag{4.1}$$

where L is the Lagrangian of the system. The Lagrangian L can be separated into a fluid component and a magnetic component:

$$L \doteq L_{\text{fluid}}[\xi, \phi] + L_{\text{B}}[\xi, \psi], \tag{4.2}$$

where

$$L_{\text{fluid}} \doteq \int_D \int_{\xi}^{+\mathsf{L}} \rho \left[\frac{\partial}{\partial t}\phi - \frac{1}{2}(\boldsymbol{\nabla}\phi)^2 - gz \right] \mathrm{d}z \, \mathrm{d}^2\mathbf{x}, \tag{4.3}$$

$$L_{\text{B}} \doteq \frac{1}{8\pi} \int_D \int_{-\mathsf{L}}^{\xi} |\mathbf{B}_0 + \boldsymbol{\nabla}\psi|^2 \, \mathrm{d}z \, \mathrm{d}^2\mathbf{x}. \tag{4.4}$$

In the above, $\xi(t, \mathbf{x})$ is a field describing the fluid–magnetic-field interface, ϕ is the flow potential for the velocity field $\mathbf{v} \doteq -\boldsymbol{\nabla}\phi$, $\mathbf{B}_0$ is a background magnetic field, ψ is a potential to describe the perturbations of the magnetic field so that $\mathbf{B} = \mathbf{B}_0 + \boldsymbol{\nabla}\psi$, and g is the acceleration of the fluid. Also, L serves as constant to denote the upper and lower boundary of the domain along the z axis. The integration domain D is a $d_x \times d_y$ periodic box in the xy plane.

For the sake of completeness, let us verify that the action (4.1) indeed leads to the nonlinear equations for MRTI. Varying the action with respect to the flow potential ϕ gives two equations. Inside the fluid slab $[z > \xi(t, \mathbf{x})]$, one finds that the flow potential satisfies Laplace's equation

$$\boldsymbol{\nabla}^2 \phi = 0. \tag{4.5}$$

This is the incompressibility condition. At the fluid interface, where $z = \xi(t, \mathbf{x})$, we find the nonlinear advection equation of the fluid interface:

$$\left[\partial_t \xi - \boldsymbol{\nabla}\phi \cdot \boldsymbol{\nabla}\xi + \partial_z \phi \right]_{z=\xi} = 0. \tag{4.6}$$

In a similar manner, when varying the action with respect to the magnetic potential ψ, we obtain two equations. In the vacuum region $[z < \xi(t, \mathbf{x})]$, the magnetic potential satisfies Laplace's equation

$$\boldsymbol{\nabla}^2 \psi = 0. \tag{4.7}$$

Along the interface $[z = \xi(t, \mathbf{x})]$, we find that the magnetic field $\mathbf{B} = \mathbf{B}_0 + \boldsymbol{\nabla}\psi$ is parallel to the surface of the perfectly conducting fluid:

$$\boldsymbol{\nabla}(\xi - z) \cdot [\mathbf{B}_0 + \boldsymbol{\nabla}\psi]_{z=\xi} = 0. \tag{4.8}$$

Finally, when varying the action with respect to the field ξ, we obtain

$$\rho \left[\frac{\partial}{\partial t}\phi - \frac{1}{2}(\boldsymbol{\nabla}\phi)^2 - gz \right]_{z=\xi} = \frac{1}{8\pi} \left| \mathbf{B}_0 + \boldsymbol{\nabla}\psi \right|^2_{z=\xi}, \tag{4.9}$$

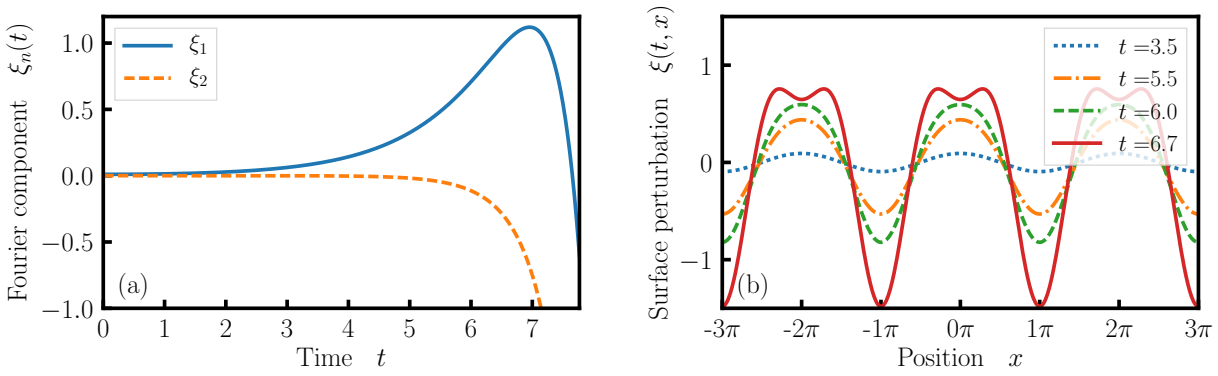

Figure 4-2. (a) Time evolution of the first and second harmonics of the MRT instability. (b) Surface perturbation $\xi(t,x)$ evaluated at different times. In this example, the fundamental wavenumber is $k = 1$, and the gravity constant is $g = 1$. The initial conditions are $\xi_1(0) = 0.01$, $\xi_2(0) = 0$, and $\Phi_{1,2}(0) = 0$. Here the strength of the magnetic field was chosen so that $\sigma \doteq (\mathbf{k}\cdot\mathbf{v}_A)^2/(kg) = 0.3$.

which serves as the dynamical equation for the fluid flow potential ϕ.

In order to obtain a tractable weakly nonlinear model for MRTI, the dynamical fields (ξ, ϕ, ψ) were expressed in terms of Fourier components as it is usually done in weakly-nonlinear analyses for the RT instability [113; 114; 115; 116; 117; 118; 119; 120]. The corresponding Fourier series were substituted into the Lagrangian, and the Lagrangian was then truncated up to a certain order in an asymptotic parameter. Once the approximated Lagrangian was obtained, the corresponding equations of motion for the wNL MRTI were derived by varying the approximated action. This procedure provided a systematic approach to study wNL MRTI and lead to a set of Hamiltonian equations that self-consistently conserve the energy of the system.

As an example, the wNL Lagrangian for the MRTI that includes the interaction of the first and second MRT harmonics is given by [3]

$$L \simeq \sum_{n=1}^{2} \left(\Phi_n \frac{\mathrm{d}\xi_n}{\mathrm{d}t} \right) - H(t, \xi_1, \xi_2, \Phi_1, \Phi_2), \tag{4.10}$$

where the Hamiltonian H is

$$H \simeq \sum_{n=1}^{2} \left(\frac{nk}{2}\Phi_n^2 - \frac{\gamma_{n\mathbf{k}}^2}{2nk}\,\xi_n^2 \right) - \frac{k^3}{8}\,\xi_1^2\,\Phi_1^2 + \frac{k^2}{2}\,\xi_2\,\Phi_1^2 - \frac{1}{2}(\mathbf{k}\cdot\mathbf{v}_A)^2\,\xi_1^2\xi_2 - \frac{k}{8}(\mathbf{k}\cdot\mathbf{v}_A)^2\,\xi_1^4. \tag{4.11}$$

Here ξ_n are the Fourier components of the fluid–magnetic-field interface and Φ_n are the Fourier components of the flow potential evaluated at the surface. Note that the latter act as canonical conjugate variables of the Fourier components ξ_n. Also, $\gamma_{n\mathbf{k}} \doteq [gk - (\mathbf{k}\cdot\mathbf{v}_A)^2]^{1/2}$ is the linear growth rate for MRTI, and $\mathbf{v}_A$ is the Alfven velocity associated to the background magnetic field $\mathbf{B}_0$. The equations of motion for the first and second Fourier coefficients are obtained by varying the action $\Lambda = \int_{t_1}^{t_2} L\,\mathrm{d}t$ using the Lagrangian (4.10). The resulting

equations are the following:

$$\delta\Phi_1: \quad \frac{\mathrm{d}\xi_1}{\mathrm{d}t} = k\Phi_1 - \frac{k^3}{4}\xi_1^2\Phi_1 + k^2\xi_2\Phi_1, \tag{4.12}$$

$$\delta\Phi_2: \quad \frac{\mathrm{d}\xi_2}{\mathrm{d}t} = 2k\Phi_2, \tag{4.13}$$

$$\delta\xi_1: \quad \frac{\mathrm{d}\Phi_1}{\mathrm{d}t} = \frac{\gamma_{\mathbf{k}}^2(t)}{k}\xi_1 + \frac{k^3}{4}\xi_1\Phi_1^2 + (\mathbf{k}\cdot\mathbf{v}_A)^2\xi_1\xi_2 + \frac{k}{2}(\mathbf{k}\cdot\mathbf{v}_A)^2\xi_1^3, \tag{4.14}$$

$$\delta\xi_2: \quad \frac{\mathrm{d}\Phi_2}{\mathrm{d}t} = \frac{\gamma_{2\mathbf{k}}^2(t)}{2k}\xi_2 - \frac{k^2}{2}\Phi_1^2 + \frac{1}{2}(\mathbf{k}\cdot\mathbf{v}_A)^2\xi_1^2. \tag{4.15}$$

These are the governing equations for the double-harmonic wNL MRTI. Note that the first terms on the right-hand side are the usual linear terms that appear from a linear analysis of the MRTI. The rest of the terms represent nonlinear couplings between the harmonics.

To discuss the temporal dynamics described by Eqs. (4.12)–(4.15), it is perhaps more instructive to discuss the Hamiltonian H rather than the equations themselves. When one varies the action, the terms inside the sum in Eq. (4.11) lead to the linear terms appearing in Eqs. (4.12)–(4.15). The next two terms in Eq. (4.11) are the nonlinear coupling terms arising from the kinetic part of the Hamiltonian H. The term proportional to $\xi_1^2\,\Phi_1^2$ represents a nonlinear self-coupling of the first harmonic, and the term containing $\xi_2\,\Phi_1^2$ describes a coupling between the first and second MRT harmonics. For the case of classical RTI, the latter is, in fact, responsible for the nonlinear driving of the second harmonic by the first harmonic. The last two terms in Eq. (4.11) contain nonlinear coupling terms of magnetic origin. Similarly to before, the first term proportional to $\xi_1^2\xi_2$ represents a coupling between the two MRTI modes, and the second term containing ξ_1^4 represents a nonlinear self-coupling of the first harmonic. It is worth noting that, contrary to the lowest-order contribution of the magnetic energy (which is stabilizing), the magnetic self-coupling term proportional to ξ_1^4 appears to be MRT destabilizing due to its negative sign.

Figure 4-2 presents the temporal evolution of the Fourier coefficients ξ_1 and ξ_2 and of the surface perturbation $\xi(t,x)$ using Eqs. (4.12)–(4.15). During the first one or two e-folding times, the amplitude of the first MRTI mode is small, and ξ_1 grows exponentially [see Fig. 4-2(a)]. As the fundamental MRT mode becomes sufficiently strong, it eventually begins to drive the second MRT harmonic. When the nonlinear self-coupling and coupling with the second harmonic are no longer negligible, ξ_1 reaches a maximum and then rapidly decreases. The resulting surface perturbation is shown in Fig. 4-2(b). Due to the presence of the second harmonic, bubble and spike structures appear on the surface perturbation. Note, however, that the rounding of the bubbles begins to deform for $t \gtrsim 6.7$. This behavior is not physical and signals the breakdown of wNL theory [121]. In terms of the time evolution of the first harmonic ξ_1, the breakdown of wNL theory roughly coincides with the inflection point for ξ_1. The dynamics beyond this point is no longer physical.

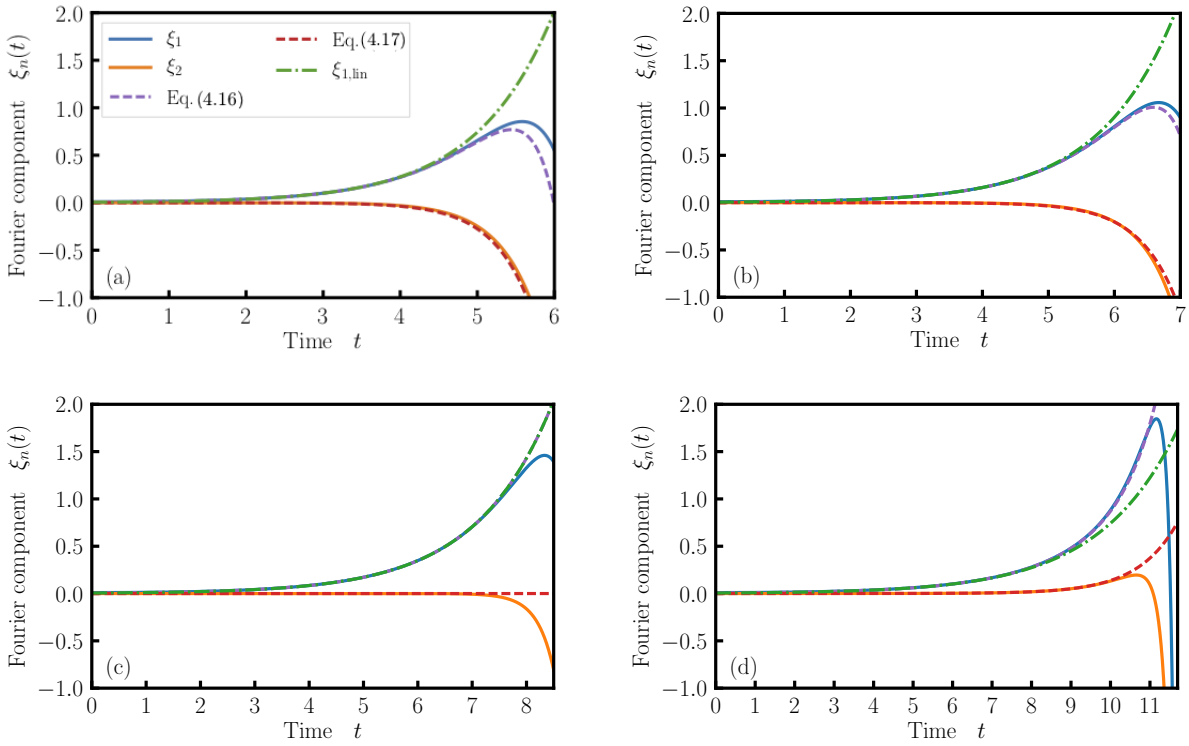

Figure 4-3. Comparison between the asymptotic expressions in Eqs. (4.16)–(4.17) and the numerical solutions of Eqs. (4.12)–(4.15). Same initial conditions and parameters were used as in Fig. 4-2. The subfigures respectively correspond to $\sigma = \{0.0, 0.25, 0.5, 0.75\}$.

4.3. Main result #2: Effects of the magnetic field on the saturation of the linear exponential growth

In contrast to linear theory, wNL theory allows to compute the limit of validity of the asymptotic expansion. To do so, one must analytically calculate the temporal behavior of the solutions of Eqs. (4.12)–(4.15) far from the transient phase but before the breakdown of wNL theory. For constant g and $\mathbf{B}_0$ and with initial conditions such that only ξ_1 is initially nonzero, it is shown in Ref. [3] that the corresponding asymptotic solutions of Eqs. (4.12)–(4.15) are given by

$$\xi_1 \sim \xi_{1,\mathrm{lin}}(t)\left(1 - \frac{k(kg+\gamma_{\mathbf{k}}^2)\gamma_{2\mathbf{k}}^2}{16g\gamma_{\mathbf{k}}^2}\left[\xi_{1,\mathrm{lin}}(t)\right]^2\right), \tag{4.16}$$

$$\xi_2 \sim -\frac{\gamma_{2\mathbf{k}}^2}{4g}\left[\xi_{1,\mathrm{lin}}(t)\right]^2, \tag{4.17}$$

where $\xi_{1,\mathrm{lin}}(t) \doteq (1/2)\xi_1(0)\exp(\gamma_{\mathbf{k}}t)$ is the dominant component of the linear solution of ξ_1.

In Fig. 4-3, the asymptotic expressions obtained in Eqs. (4.16) and (4.17) are compared to the numerical solutions of Eqs. (4.12)–(4.15) using different values for the parameter $\sigma \doteq (\mathbf{k}\cdot\mathbf{v}_A)^2/(kg)$, which measures the stabilizing effect of the external magnetic field on the MRTI. In all cases, the asymptotic expressions approximate well the numerical solutions for times before the breakdown of wNL theory; i.e., in the temporal window after the transient phase and to the saturation of the growth of ξ_1. In particular, Fig. 4-3(c) shows the case for $\sigma \simeq 1/2$ where the growth rate $\gamma_{2\mathbf{k}}^2$ for the second MRTI harmonic is zero. As expected, the second Fourier component ξ_2 lies close to zero until late times, and the Fourier component ξ_1 closely follows the linear growth. As shown in Fig. 4-3(d), where $\sigma = 0.75$, the numerical solution for ξ_1 and its asymptotic approximation indeed grow faster than the linear approximation $\xi_{1,\mathrm{lin}}$. This confirms the remark given in the previous paragraph.

One way to evaluate the strength of nonlinear effects is to measure the difference between the linear and nonlinear solutions for the MRTI [114]. When this difference becomes large, the asymptotic series used by the wNL theory usually breaks down, and the description is no longer valid. Let us determine then the regime of validity of the present wNL theory. Let the saturation amplitude (SA) be defined as the amplitude $\xi_{1,\mathrm{sat}}$ of the linear MRT solution calculated at the time when the nonlinear solution differs by 10%, i.e., when $|\xi_{1,\mathrm{lin}} - \xi_1|/\xi_{1,\mathrm{lin}} = 0.1$ [122; 115]. Using this definition and substituting Eq. (4.16) leads to

$$k\xi_{1,\mathrm{sat}} = \sqrt{\frac{2}{5}}\, f(\sigma) \simeq 0.63 f(\sigma), \tag{4.18}$$

where

$$f(\sigma) \doteq \sqrt{\left|\frac{1-\sigma}{(1-2\sigma)(1-\sigma/2)}\right|} \tag{4.19}$$

is a function capturing the effects of the magnetic tension on the MRT saturation amplitude. In terms of the MRT wavelength, Eq. (4.18) can be written as $\xi_{1,\mathrm{sat}} \simeq 0.1\lambda f(\sigma)$.

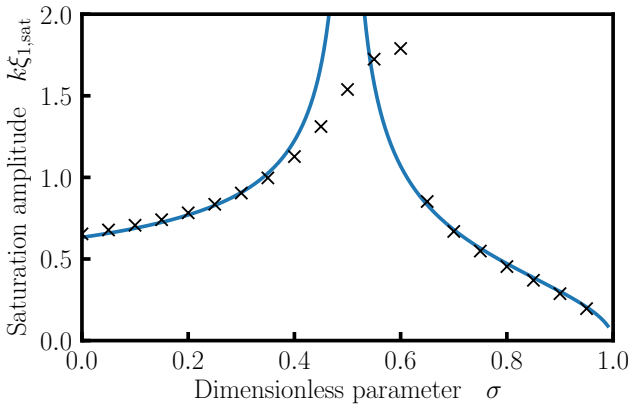

Figure 4-4. Saturation amplitude $k\xi_{1,\mathrm{sat}}$ as a function of the parameter σ. The continuous line is given by Eq. (4.18). The scatter points correspond to measured SAs obtained from numerical simulations which used $k = 1$ and $g = 1$. The initial conditions were $\xi_1(0) = 0.001$, $\xi_2(0) = 0$, and $\Phi_{1,2}(0) = 0$.

The SA can be used to denote the limit of validity of wNL theory beyond which nonlinear effects become strong. As an example, for the pure RTI case with no magnetic-field tension ($\sigma = 0$), one has $\xi_{1,\mathrm{sat}} \simeq 0.1\lambda$ which agrees with previously reported results [122; 115; 114]. Note that, when the fundamental mode has reached the SA for the unmagnetized case, the second harmonic has grown to $|\xi_2/\xi_{1,\mathrm{sat}}| \simeq 0.31$, in other words, almost a third of the fundamental harmonic.

The SA calculated in Eq. (4.18) is plotted in Fig. 4-4 as a function of the dimensionless parameter σ. The analytically calculated SA is also compared to measured SAs obtained via numerical solutions of Eqs. (4.12)–(4.15). For the cases with magnetic-field tension, the calculated SA shows good agreement for $\sigma \in [0, 0.4] \cup [0.6, 1)$. For $0 \leq \sigma \leq 0.4$, the SA remarkably increases as the magnetic-field tension becomes larger. It is interesting that, although the magnetic-field tension stabilizes the linear growth of MRTI, it can also increase the SA at which the linear MRTI transitions to the nonlinear phase. Note that a similar effects happens in the case of the RT instability when the effects of surface tension are included Ref. [119]. Remarkably as well, Fig. 4-4 shows that, for $0.6 \leq \sigma \leq 1.0$, the SA decreases as the magnetic-field tension increases. It actually falls below the saturation amplitude of the pure RT case. This trend is not yet fully understood.

In the interval $0.4 \leq \sigma \leq 0.6$ in Fig. 4-4, the calculated SA differs substantially from the measured SA obtained from simulations. This occurs because the nonlinear correction term in Eq. (4.16) tends to zero near $\sigma \simeq 0.5$ which in turn leads to the divergence of $f(\sigma)$. [In fact, one can see in Fig. 4-3(c) that the linear and wNL solutions are almost identical throughout a large portion of the evolution of the MRTI.] To fix this issue, one would have to calculate higher-order corrections to the asymptotic solutions given in Eqs. (4.16) and (4.17). However, doing so would lead to terms that go beyond the accuracy of the theory (4.10), so their significance would be questionable. Correcting this issue has been left for future work.

4.4. Conclusions and future work

The work published in Ref. [3] proposes a theoretical model to describe the weakly nonlinear magnetic Rayleigh–Taylor instability (MRTI). The model is obtained by identifying an exact action for the MRTI, approximating the MRTI Lagrangian, and then varying the action to derive the governing approximated equations. The obtained wNL theory includes the generation of MRT coupling and describes the emergence of MRT bubbles and spikes. It is found that the amplitude at which the linear and weakly nonlinear solutions begin to diverge depends on the stabilizing effect of the magnetic-field tension.

The present theoretical work can be extended to study the MRTI in more complex settings. Since the Lagrangian for MRTI can be considered universal and independent of the geometry considered, future research directions include studying MRTI in finite-width planar slabs and in cylindrical shells with finite thickness. Such work could be useful to compare weakly nonlinear theory to the experimental observations on the MRT instability reported in Refs. [77; 78; 81]. Excitingly too, this methodology for deriving wNL theories for interfacial instabilities is also applicable to study the Richtmyer–Meshkov instability that is observed at Sandia's "Decel" experimental campaign on the Z machine [123]. These directions of future research can also be complemented with detailed MHD simulations using the code Hydra. After having learned how to use Hydra during this last stretch of my fellowship, it would be interesting to compare the results from this line of theoretical work to detailed numerical simulations and to experiment.

5. CONSERVATIVE SCALING OF MAGNETO INERTIAL FUSION TARGETS TO LARGER PULSED-POWER DRIVERS

5.1. Introduction

For the last 60 years, achieving ignition and high neutron yields in the laboratory has remained an elusive goal for plasma-physics research. Besides the well-known approach based on magnetic-confinement fusion, one potential avenue for reaching this scientific milestone is inertial confinement fusion (ICF). In the traditional laser-driven approach to ICF, powerful lasers are utilized to directly or indirectly energize the outside surface of spherical capsules in order to achieve high ablation pressures ($\sim$ 100 Mbar) and implosion velocities greater than $\sim$ 400 km/s. In contrast, magneto-inertial fusion (MIF) relaxes these stringent fuel conditions by the introduction of strong magnetic fields in the fuel, which in turn modify the transport properties within the fuel.

One particular MIF concept is the Magnetized Liner Inertial Fusion (MagLIF) platform [73], which is currently being studied at the pulsed-power Z facility at Sandia National Laboratories [124; 74; 75; 125]. The Z facility delivers a strong $\sim$18-MA electrical current pulse to the cylindrical MagLIF target, which then implodes under the action of the $\mathbf{J} \times \mathbf{B}$ force. Since MagLIF utilizes a relatively thick and heavy metallic cylindrical tamper, or liner, the achievable implosion velocities are $70 - 150$ km/s, which are substantially lower to those in traditional ICF. Therefore, since the fuel is not shock-heated, a 2–4-kJ 1-TW laser is used to preheat the fuel in order to achieve an efficient adiabatic compression [58; 57]. Moreover, since the implosions are considerably slower (in the order of 100 ns), the fuel must be premagnetized in order to reduce deleterious thermal conduction losses. This is achieved by external pulsed coils which provide a 10–20 T, predominantly axial magnetic field. The successful combination of these key ingredients in laboratory experiments has led to significant thermonuclear yield production [75; 124] and significant plasma magnetization inferred via secondary DT neutron emission [126; 127].

Given the relative success of the MagLIF platform and its interesting demonstrated confinement parameter $P\tau \sim 0.8$ Gbar-ns at $\sim$ 16 MA peak current [125], there has been a strong interest in scaling the platform to higher peak currents, specifically to 45 MA or even 60 MA. However, scaling the MagLIF platform is not entirely straightforward. The space of basic design parameters describing MagLIF is at least eight dimensional (see Fig. 5-1). Apart from the delivered peak current, parameters include the curent rise time, the liner outer radius, the liner aspect ratio (AR), the liner material, the height of the target, the delivered preheat energy, the imposed external magnetic field, and the initial fuel density. Given the necessity to explore a relatively large parameter space, scoping future MagLIF

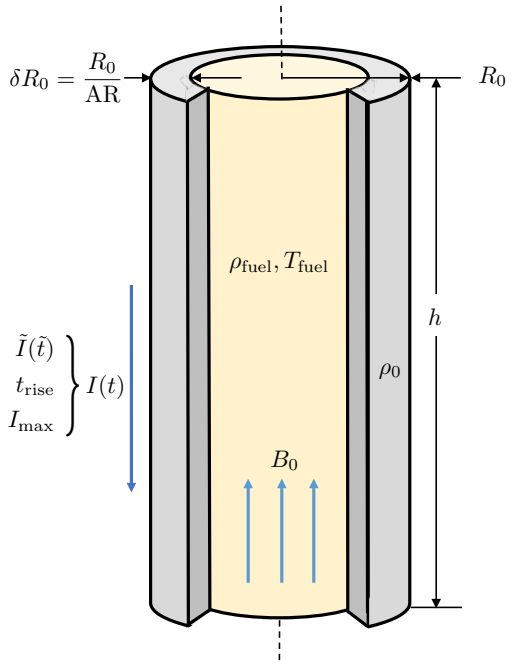

Figure 5-1. Schematic diagram with the main parameters characterizing a MIF target. In the conservative scaling approach, we uniquely determine how these parameters scale as functions of the maximum current Imax delivered to the target.

designs at higher peak currents with present-day rad-MHD modeling tools can indeed become overwhelming.

Nevertheless, several studies have explored the potential for MagLIF to generate high fusion yields on future, higher-energy pulsed-power drivers [72; 74; 128; 129; 130]. Often, these studies assume constraints on certain design parameters such as the current rise-time of the pulsed-power generator, the target height, the liner AR, the liner material (usually Breyllium or Gold in some cases), and the external magnetic field B_0 in order to reduce the dimensionality of the design space. Then, the remaining basic target parameters (target outer radius, fuel preheat, and initial fuel densities) are explored, and an optimized configuration is sought that maximizes the neutron yield or energy gain of the target implosions at a given peak current [128; 130]. This so-called "optimized scaling" approach has been obtained from hundreds of 1D LASNEX simulations. Excitingly, this approach predicts 1-MJ DT yields at ~ 35 MA and ~ 50 MJ at ~ 60 MA for MagLIF (see Fig. 5-2)].

In this work, we proposed a new philosophy to "conservatively" scale general MIF targets, including MagLIF, to higher peak currents. Our scaling philosophy is inherently different from the "optimized" scaling approach. Instead of maximizing yield or energy gain at a given peak current, we propose to identify scaling strategies that preserve much of the physics regimes already known or being studied on today's Z pulsed-power driver. By avoiding significant deviations into unexplored and/or less well-understood regimes, we reduce the risk of unexpected outcomes on future scaled-up experiments. Our approach seeks to

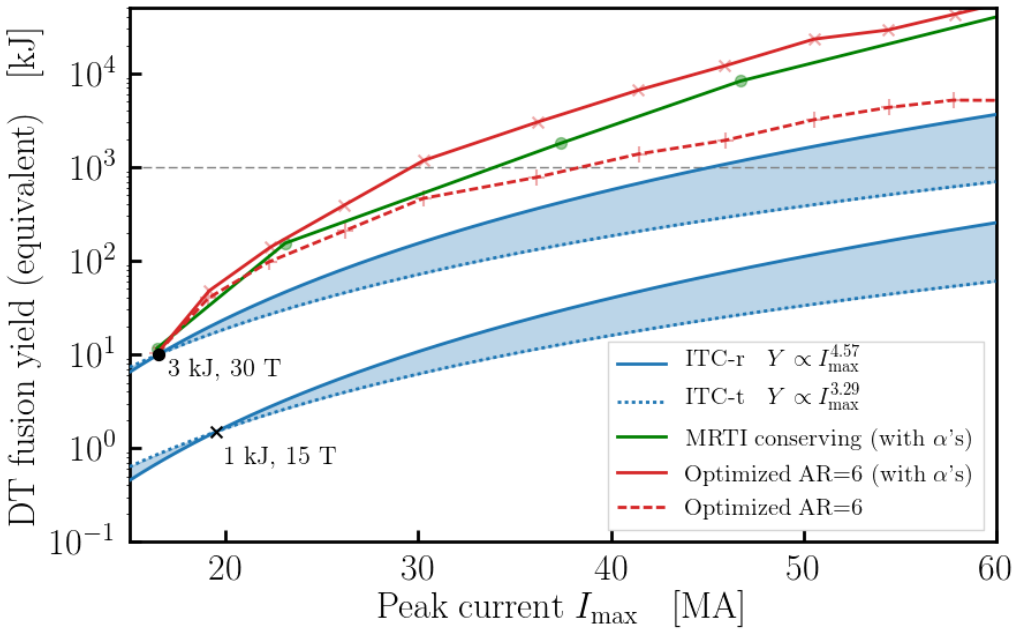

Figure 5-2. DT fusion yield as a function of peak electrical current following several proposed scaling strategies for the MagLIF platform. The red curves are obtained from the optimized scaling approach assuming a AR6 liner. Predicted yields with and without alpha heating are included. The green curve represents a newly developed optimized scaling study that intends to conserve the liner stability towards the MRTI. Finally, the blue curves and their shaded regions represent the expected scaling laws using the ITC-t and ITC-r scaling paths.

build confidence in the scaling potential for MIF by minimizing extrapolations away from the most robustly studied neighborhoods of parameter space accessible to present-day experiments. Another advantage of our approach is that it provides a one-to-one correspondence between targets across driver energy scales; in other words, all the parameters characterizing a MIF target are given as functions of the peak current for each scaling path considered. Our main results are two-fold. First, we developed a scaling framework from which we can explore different scaling strategies for future MIF targets. Second, from a subset of these scaling strategies, we studied the scaling of the target parameters, the expected performance, and the key mechanisms that affect target performance (e.g., magnetohydrodynamic instabilities, impurity mix, radiation losses, thermal conduction losses, bulk mass flow losses, magnetic flux losses, alpha heating, and laser-plasma instabilities). Details of these findings are reported in Ref. [4].

5.2. Main result #1: Development of a current-scaling framework

The current-scaling framework that we proposed in Ref. [4] relied on four ideological pillars: conserve the implosion dynamics via self-similar scaling, conserve the liner material, conserve the liner resilience towards the magneto Rayleigh–Taylor instability (MRTI), and conserve or even improve the physics regimes and transport of the fuel at stagnation. Below, I shall comment on the models used and identify key dimensionless parameters that describe a general MIF system including MagLIF.

For a relatively highly converging target such as MagLIF, it is important that future scaled-up MagLIF targets do not increase their convergence at stagnation. As it is well-known, highly converging ICF targets can be affected by (i) the MRTI that could shred the liner and compromise the inertial confinement or by (ii) catastrophic mix from the liner material that can cool down the hot fuel region [125]. To place these ideas into a mathematical framework, in Ref. [4], we used a simple thin-shell model to describe the liner implosion. The liner is driven by an external magnetic pressure source, and it is pushed from the interior by an adiabatically compressed fuel. Upon introducing dimensionless variables, we found two key dimensionless parameters that describe the implosion dynamics:

$$\Pi \doteq (10)^{-8}\frac{[I_{\max}(\mathrm{MA})]^2\cdot[t_{\mathrm{rise}}(\mathrm{ns})]^2}{[\widehat{m}(\mathrm{g/cm})]\cdot[R_0(\mathrm{cm})]^2}, \tag{5.1}$$

$$\Phi \doteq 1.33\cdot(10)^{-8}\frac{[E_{\mathrm{preheat}}(\mathrm{kJ})]\cdot[t_{\mathrm{rise}}(\mathrm{ns})]^2}{[\widehat{m}(\mathrm{g/cm})]\cdot[h(\mathrm{cm})]\cdot[R_0(\mathrm{cm})]^2}. \tag{5.2}$$

Here $I_{\max}$ is the peak electrical current, t_{rise} is the rise time of the current pulse, $\widehat{m}$ is the mass per-unit-length of the liner, R_0 is the liner outer radius, E_{preheat} is the preheat energy delivered to the fuel, and h is the target height. The dimensionless parameter Π describes the magnetic drive acting upon the liner. As an example, larger peak currents and less massive liners will be driven harder or accelerated faster. This translates into a larger Π parameter. Similarly, the dimensionless parameter Φ describes the amount of preheat energy delivered to the fuel. More preheat energy will cause the fuel to push back on the imploding liner at

larger radii (or equivalently, smaller convergence ratios). According to the thin-shell model, in order to maintain the dimensionless acceleration history of the liner and the eventual convergence ratio of stagnation, it is necessary to have

$$\Pi = \text{const}, \qquad \Phi = \text{const}, \tag{5.3}$$

when scaling up in peak current $I_{\max}$. These two equations represent two constraints for the scaling of the parameters appearing in Eqs. (5.1) and (5.2).

The second pillar for conservative scaling originates from the fact that all ICF approaches are sensitive to material models, such as equations of state, radiation opacities, and electrical and thermal conductivities. Establishing a credible scaling path for MIF requires demonstrating sufficient understanding of the materials used. To avoid unnecessary uncertainties associated with new material models, our scaling approach considers the same materials used in present-day experiments across all proposed scales. In terms of the simple thin-shell implosion model, this amounts to fixing the liner initial density so that

$$\rho_0 = \text{const}. \tag{5.4}$$

MIF implosions are subject to hydrodynamic instabilities that threaten to disrupt the integrity of the imploding liner near stagnation and reduce the associated energy confinement time for the hot fusion fuel [76]. Hydrodynamical instabilities are also believed to seed the unwanted mix from the liner to the hot fuel region. In practice, the effects of instabilities are reduced by choosing an appropriate initial liner AR to ensure a sufficiently stable tamper during the fusion burn. The third pillar of conservative scaling intends to conserve the robustness of MIF liners to these instabilities. A simple calculation given in Ref. [4] shows that the growth of the most dangerous MRT modes in the interior of the liner depends on three factors: the dimensionless acceleration history, the convergence ratio (CR) of the implosion, and the liner in-flight aspect ratio (IFAR). Since we strive to maintain the self-similar implosion trajectories for the liner, the first two factors are automatically conserved by our scaling approach. The third factor, the liner IFAR, is essentially the time-dependent ratio of the liner radius to its thickness. Intuitively, a liner with larger IFAR is more prone to be affected by hydrodynamical instabilities since its relative thickness is smaller. Using an adiabatic compression model for the liner and a simple momentum-conservation model, it is shown in Ref. [4] that the dimensionless parameter that characterizes the magnitude of the IFAR is given by

$$\Psi \doteq 0.062 \left(\frac{\gamma-1}{\gamma}\right) \frac{[R_0(\text{mm})]^2\ [\rho_{\text{ref}}(\text{g/cm}^3)]}{[\widehat{m}(\text{g/cm})]} \left(\frac{[I_{\max}(\text{MA})]^2}{2\pi\ [R_0(\text{mm})]^2\ [P_{\text{ref}}(\text{Mbar})]}\right)^{1/\gamma}, \tag{5.5}$$

where γ is the adiabatic parameter for the liner, ρ_{ref} is the liner reference density, and P_{ref} is the reference pressure. These parameters enter the adiabatic equation of state for the liner: $P = P_{\text{ref}}(\rho/\rho_{\text{ref}})^\gamma$. Since our conservative scaling strategy advocates for the usage of the same liner materials, the previous liner parameters are assumed to remain fixed when scaling to higher peak currents. Therefore, in order to maintain the robustness of a MIF liner to hydrodynamical instabilitites, it is necessary to conserve the following ratio:

$$\Psi \propto \frac{R_0^2}{\widehat{m}} \left(\frac{I_{\max}}{R_0}\right)^{2/\gamma} = \text{const}. \tag{5.6}$$

MIF systems may suffer from various energy-loss mechanisms, including radiation, conduction, and end losses, that may prohibit the fuel from reaching the expected fuel conditions at stagnation. In this regard, the final pillar for conservative scaling is that, for future scaled-up MIF targets, the physics regimes of the fusion fuel near stagnation should not depart too much from those diagnosed in present-day experiments. More specifically, we strive to conserve the relative importance of the energy-loss channels to the PdV work done on the fuel. Based on Ref. [72], it can be shown that the dimensionless parameters characterizing radiation losses, electron-conduction losses, ion-conduction losses, and end-losses can be written respectively as follows:

$$\Upsilon_{\rm rad} \doteq 9.623 \cdot (10)^4 \frac{[\rho R(\mathrm{g/cm^2})]^2 \cdot [T(\mathrm{keV})]^{1/2} \cdot [t_{\rm rise}(\mathrm{ns})]}{[\widehat{U}(\mathrm{kJ/cm})]}, \tag{5.7}$$

$$\Upsilon_{\rm ce} \doteq 2.753 \, \frac{[T(\mathrm{keV})]^{7/2} \cdot [t_{\rm rise}(\mathrm{ns})]}{[\widehat{U}(\mathrm{kJ/cm})]} g_e(x_e), \tag{5.8}$$

$$\Upsilon_{\rm ci} \doteq 4.064 \cdot (10)^{-2} \frac{[T(\mathrm{keV})]^{7/2} \cdot [t_{\rm rise}(\mathrm{ns})]}{[\widehat{U}(\mathrm{kJ/cm})]} g_i(x_i), \tag{5.9}$$

$$\Upsilon_{\rm end} \doteq 4.595 \cdot (10)^3 \frac{[\rho R^2(\mathrm{g/cm})] \cdot [T(\mathrm{keV})]^{3/2} \cdot [t_{\rm rise}(\mathrm{ns})]}{[\widehat{U}(\mathrm{kJ/cm})][h(\mathrm{cm})]}, \tag{5.10}$$

where $\widehat{U}$ is the internal energy of the fuel per-unit-length. The functions $g_e(x_e)$ and $g_i(x_i)$ are functions that depend on the electron and ion Hall parameters and describe the degree of magnetization of the fusion fuel. The parameters above are evaluated at plasma conditions near stagnation. When these parameters are small, the relative importance of the corresponding loss channel is low. When scaling MIF targets, it is important to understand how these parameters will scale at higher peak currents.

The dimensionless parameters in Eqs. (5.7)–(5.10) also provide an intuitive overview of the various choices that can be made when designing a MIF platform. For example, it is well known that, at fixed stagnation pressures, MIF targets with higher fuel temperatures will perform better due to the strong dependence of the fusion reactivity on fuel temperature. Therefore, when scaling MIF targets to larger pulsed-power drivers, one possibility is to scale the initial fuel density and the preheat energy in such a way that higher temperatures at stagnation are achieved. However, as shown in Eqs. (5.8)–(5.10), increasing the fuel temperature alone may lead to larger conduction losses and end losses, which could prevent the fuel from reaching the desired state at stagnation. However, Eqs. (5.8)–(5.10) also tell a MIF-target designer how to mitigate those risks. Specifically, electron conduction losses can be held at bay by increasing the external magnetic field, which enters the electron Hall parameter x_e. [In the highly magnetized regime, $g_e(x_e) \propto x_e^{-2} \propto (B_0 T^{3/2}/\rho)^{-2}$.] When the fuel temperature rises, end losses increase because the ion acoustic velocity, which sets the characteristic speed of the rarefraction wave exiting the ends of the liner, will increase. To mitigate this effect, the target height h appearing in the denominator of Eq. (5.10) must be increased. This is only one example of a specific scaling strategy where the fuel temperature is increased with peak current. More detailed discussions on other scaling strategies are given in Ref. [4].

Table 5-1. Summary of the specific scaling strategies for MIF target parameters that were investigated in the current-scaling work. One convenience of the conservative scaling theory is that explicit expressions are given for the scaling of all the relevant quantities characterizing a MIF target.

Target parameter $(\alpha, \beta, \epsilon, \xi)$	ITC-t $(0, 0, {}^{9}/_{7}, {}^{9}/_{7})$	ITC-r $(0, {}^{3}/_{7}, {}^{3}/_{7}, 0)$
Liner density	const	const
Rise time	const	const
Initial target radius	$I_{\max}^{5/14}$	$I_{\max}^{5/14}$
Liner mass per-unit-length	$I_{\max}^{9/7}$	$I_{\max}^{9/7}$
Aspect ratio (thin-shell limit)	$I_{\max}^{-4/7}$	$I_{\max}^{-4/7}$
Preheat pressure	$I_{\max}^{9/7}$	$I_{\max}^{9/7}$
Target height	const	$I_{\max}^{3/7}$
Fuel density	$I_{\max}^{9/7}$	$I_{\max}^{3/7}$
Fuel temperature	const	$I_{\max}^{6/7}$
Preimposed magnetic field	$I_{\max}^{9/7}$	const

5.3. Main result #2: Identifying viable scaling strategies and calculating the expected gains in performance

From the dimensionless parameters introduced in the previous section, we identified several specific scaling paths that satisfied the majority of the constraints imposed [4]. For the sake of brevity, in this report, I shall only discuss the implosion-time conserving (ITC) scaling paths, which assume a constant rise time $t_{\text{rise}} \simeq 100$ ns for future pulsed-power drivers.

Table 5.2 shows the obtained scaling laws for the main parameters describing a MIF target. The second and third columns contain the scaling laws for the implosion-time–conserving, temperature-conserving (ITC-t) scaling path and implosion-time–conserving, temperature-conserving (ITC-r) scaling path, respectively. In terms of the parameters describing the liner itself, both strategies have the same scaling laws. Some interesting trends to note are that, in general, MIF targets will tend to be grow radially ($R_0 \propto I_{\max}^{5/14}$) when increasing the peak current $I_{\max}$. The liners themselves will also be subject to larger magnetic pressures at higher peak currents since $P_{\text{B}} \propto I_{\max}^2/R_0^2 \propto I_{\max}^{9/7}$. In order to take into account the compression of the liner due to the higher magnetic pressure, the target AR$\doteq R_0/\delta R_0$ must decrease. (Physically, the thickness of the liners relative to the liner outer radius increases.) Another trend worth noting is that the preheat energy scales as $I_{\max}^{(2+\beta)}$, where β is the scaling exponent of the target height. This scaling law is obtained from $E_{\text{preheat}} \propto P_{\text{preheat}} R_0^2 h \propto I_{\max}^{(2+\beta)}$. For the temperature conserving ITC-t path, the scaling of the preheat energy is $E_{\text{preheat}} \propto I_{\max}^2$, while for radiation-conserving ITC-r path, the scaling is $E_{\text{preheat}} \propto I_{\max}^{2.43}$.

The ITC-t and ITC-r strategies differ in the scaling of the fuel parameters and of the preimposed magnetic field. The goal of the ITC-t path is to maintain the peak fuel temperatures when scaling to higher peak currents. This scaling strategy intends to mitigate the risk associated to unforeseen kinetic effects that might occur once the fuel temperature becomes too high. In order to maintain the fuel temperature, the ITC-t path advocates for a relatively strong scaling law for the fuel density as shown in Table 5.2. One disadvantage of the ITC-t path is that the plasma becomes more collisional at stagnation. This effectively lowers the electron Hall parameter and could increase conduction losses. In order to mitigate this effect, the ITC-t path requires an increase in the magnetic-field strength. Another disadvantage of the ITC-t path is that, by increasing the fuel density, the relative radiation losses are expected to increase. This might bring the risk of having the targets operate in a regime where radiation losses become too important. As an alternative scaling strategy, the ITC-r path is designed to keep the relative radiation losses constant. However, this comes at the expense of having to increase the fuel temperature. Due to the relative scaling between the initial fuel density and the fuel temperature, the degree of electron magnetization of the plasma increases in the ITC-r path. Therefore, this path does not require improvements in the preimposed magnetic field. (This is not entirely true when considering ions. To mitigate any risks due to increases in ion conduction, there might be a need to increase slightly the magnetic field.) A major disadvantage of the ITC-r path is that, since the fuel temperature rises, end losses are expected to increase because of the higher ion acoustic velocities. To mitigate this effect, the target height must increase in the ITC-r path. In consequence, more preheat energy needs to be delivered to the target in order to reach the required preheat pressure (because there is more fuel mass). Also, since the target initial inductance is proportional to the target height, the ITC-r path will require additional energy from the pulsed-power driver to reach the same maximum peak current as compared to targets scaled using the ITC-t strategy.

In Ref. [4], we also calculated the scaling laws of several dimensionless parameters that are commonly used to characterize hydrodynamical mixing, energy-loss channels, and other fuel-related parameters concerning transport and the potential of α heating. These scaling laws are summarized in Table 5.3. For both scaling paths, most of the dimensionless parameters characterizing various metrics of mix remain constant when scaling to higher peak currents. This is a consequence of the self-similar scaling constraint for the liner implosions that was imposed in our framework. Concerning the energy-loss channels, the ITC-t path has an unfavorable scaling for the relative radiation losses (5.7). In contrast, the ITC-r path shows unfavorable scaling laws for ion-conduction losses. (Conduction losses in the Bohm regime could be mitigated by increasing the magnetic field slightly when increasing peak current.) It is exciting to note that both scaling strategies show favorable scaling laws for plasma conditions to allow α heating. The last rows in Table 5.3 show the expected scaling laws for various fuel quantities, including the electron magnetization, Knudsen-type parameters, the Nernst effect, and parameters characterizing α heating. Ultimately, these relations provide guidance on the risks involved with each scaling law. The relations also provide information on the tradeoffs that are made when selecting a scaling path over another, or when deviating from the prescribed scaling rules presented in Table 5.2. Finally, this framework also provides guidance on what sort of experiments need to be done on present-day Z to address issues

Table 5-2. Summary of the scaling rules for the relevant characteristic parameters regarding hydrodynamical instabilities and mix, nonideal energy gain and loss mechanisms, and other fuel parameters for MIF targets. Green, yellow, and red cells respectively indicate favorable, neutral, and unfavorable scaling rules for MIF targets with higher energy drivers.

Dimensionless quantity $(\alpha, \beta, \epsilon, \xi)$	ITC-t $(0, 0, {}^{9}/_{7}, {}^{9}/_{7})$	ITC-r $(0, {}^{3}/_{7}, {}^{3}/_{7}, 0)$
Growth of most damaging MRTI modes	const	const
Normalized mix layer width ($A = 1$)	const	const
Atwood number deviation	$I_{\max}^{5/7}$	$I_{\max}^{-1/7}$
Normalized fall-line time	const	const
Relative radiative loss ratio	$I_{\max}^{9/7}$	const
Electron relative conductive loss ratio (magnetized)	$I_{\max}^{-2}$	$I_{\max}^{-5/7}$
Ion relative conductive loss ratio (unmagnetized)	$I_{\max}^{-2}$	$I_{\max}$
Ion relative conductive loss ratio (Bohm)	$I_{\max}^{-2}$	$I_{\max}^{1/7}$
Relative end loss ratio	const	const
Relative α-heating ratio	$I_{\max}^{9/7}$	$I_{\max}^{15/7}$
Electron Hall parameter	const	$I_{\max}^{6/7}$
Plasma thermal/magnetic pressure ratio	$I_{\max}^{-9/7}$	$I_{\max}^{9/7}$
Knudsen parameter	$I_{\max}^{-9/7}$	$I_{\max}^{6/7}$
Magnetic Knudsen parameter	$I_{\max}^{-23/14}$	$I_{\max}^{1/14}$
Nernst parameter	$I_{\max}^{-2}$	$I_{\max}^{-5/7}$
Radius–α-stopping-length ratio	$I_{\max}^{23/14}$	$I_{\max}^{-1/2}$
Magnetic-field–radius product	$I_{\max}^{23/14}$	$I_{\max}^{5/14}$
α-stopping-length–axial-length ratio	$I_{\max}^{-9/7}$	$I_{\max}^{3/7}$
α-stopping-time–burn-time ratio	$I_{\max}^{-9/7}$	$I_{\max}^{6/7}$

Table 5-3. Scaling of various quantities concerning performance of MIF targets.

Performance metric $(\alpha, \beta, \epsilon, \xi)$	ITC-t $(0, 0, {}^{9}/_{7}, {}^{9}/_{7})$	ITC-r $(0, {}^{3}/_{7}, {}^{3}/_{7}, 0)$
Energy-confinement time	const	const
"no-α" Neutron yield	$I_{\max}^{3.29}$	$I_{\max}^{4.57}$
"no-α" Neutron yield per unit length	$I_{\max}^{3.29}$	$I_{\max}^{4.14}$
"no-α" Neutron yield as funct. of driver energy	$E_{\text{driver}}^{1.64}$	$E_{\text{driver}}^{1.88}$
Areal density	$I_{\max}^{0.93}$	$I_{\max}^{0.93}$
Lawson ignition parameter	$I_{\max}^{1.29}$	$I_{\max}^{2.14}$
Lawson ignition parameter as a funct. of energy	$E_{\text{driver}}^{0.64}$	$E_{\text{driver}}^{0.88}$

that might appear in future scaled-up targets.

In Ref. [4], we also calculated the expected scaling laws of various performance metrics that are usually used to characterize MIF targets. The obtained scaling laws are shown in Table 5.3. It is to be noted that the estimates on neutron yield were calculated without considering the effects of α heating. As shown, the ITC-t scaling path presents a robust $I_{\max}^{3.29}$ scaling for the neutron yield, while the ITC-r scaling path shows a more aggressive $I_{\max}^{4.57}$ scaling for the same metric. The difference between the two strategies is caused by two reasons: (1) the ITC-r scaling path leads to higher fuel temperatures which increase the fusion reactivity, and (2) the targets that scaled using the ICT-r strategy are taller and therefore have more fusion fuel. In order to remove the effects of the target height, it might be more appropriate to compare the scaling laws of the neutron yield per-unit-length or of the neutron yield as a function of energy E_{driver} delivered to the target. According to these metrics, Table 5.3 shows that there is only a slightly more favorable scaling law for yield using the ITC-r strategy. The expected scaling laws for the Lawson ignition parameter are also given in Table 5.3.

The scaling laws for neutron yield using the ITC-r and ITC-r scaling paths are plotted in Fig. 5-2. There are two comments to be made here. First, it is not surprising that the "conservative" scaling paths scale less favorably than the "optimized" scaling approach. In conservative scaling, we try to keep the scaled MIF target within the same physical operating regimes as present-day targets. Optimized scaling intends to maximize performance at each peak current. Second, Fig. 5-2 shows that the present-day highest performing MagLIF experiments will not scale to MJ yields within the framework of conservative scaling. There might be a possibility of reaching the 1-MJ benchmark once α heating is taken into account, but it would be extremely risky to solely rely on this effect to get over the finish line. However, Fig. 5-2 also shows that an upgraded MagLIF platform could in fact scale to multi MJs at 60 MA or lower within the conservative-scaling framework. This provides further motivation to increase the preheat energy delivered to present-day MagLIF targets and to increase the pre-imposed magnetic fields.

5.4. Conclusions and future work

In Ref. [4], we proposed a framework to conservatively scale general MIF targets to larger pulsed-power drivers. Using this framework, we derived explicit scaling laws for key parameters characterizing a general MIF target. We also derived scaling laws for key metrics characterizing the effects of hydrodynamic instabilities and mix, the effects due to various energy-loss channels, fuel properties at stagnation, target performance, and risks concerning LPI effects (not shown in this report). Overall, the proposed framework allows to intuitively evaluate the advantages and disadvantages when considering a particular scaling path.

Excitingly, this research has opened several avenues for future work. There is ongoing work to compare the derived scaling laws against detailed radiation-MHD simulations using different codes. Preliminary results show good agreement between simulations and theory. It will also be interesting to compare in detail the "optimized" scaling and "conservative" scaling approaches that are currently proposed for the MagLIF platform (see Fig. 5-2). Such exercise would provide insights into how these scaling strategies are similar and how they are different.

Surprisingly too, the developed scaling framework is not only applicable to current scaling. There are other interesting scaling paradigms for MagLIF targets that could potentially be fielded in the present-day Z machine. Two alternative scaling methodologies are currently being investigated. First, we are using the scaling framework to explore target configurations that increase the stability of MagLIF liners. When considering $I_{\max}$ and t_{rise} constants, the Π parameter in Eq. (5.1) can be conserved when maintaining the product $\widehat{m}R_0^2$ constant. This means that a target external radius can be reduced and its mass increased in order to conserve the characteristic magnetic drive. This fact highlights a particular advantange of MIF as compared to conventional laser-driven ICF: for same driving currents, reducing the initial radius of the Z pinch leads to an increase in the magnetic pressure acting upon the target. Making the liner more massive while reducing its outer radius means that the liner AR must decrease. Therefore, the liner IFAR will also decrease, so the liner will become more robust towards hydrodynamical instabilities [see Eq. (5.5)]. The second variation of the scaling framework is to explore the scaling of target parameters with respect to the liner material density ρ_0. This study could help clarify the advantages and disadvantages of fielding MagLIF liners that are made of alternative materials, such as Lithium, Copper, or even Gold. These new ideas for scaling, $\widehat{m}R_0^2$ scaling and liner density ρ_0 scaling, will continue to be investigated after the end of this LDRD project.

Last but not the least, it is worth mentioning that Z shots were awarded this year and the next to experimentally validate the current-scaling framework for the MagLIF platform. These experiments will compare predictions from the theory and simulations against experimental observables. The first shots are scheduled to occur in December 2020.

REFERENCES

[1] D. E. Ruiz, M. E. Glinsky, and I. Y. Dodin, J. Plasma Phys. **85**, 905850101 (2019).

[2] J. W. Burby and D. E. Ruiz, J. Math. Phys. pp. 1–40 (2020).

[3] D. E. Ruiz, Phys. Plasmas **27**, 022121 (2020).

[4] P. F. Schmit and D. E. Ruiz, Phys. Plasmas **27**, 062707 (2020).

[5] P. H. Diamond, S.-I. Itoh, K. Itoh, and T. S. Hahm, Plasma Phys. Control. Fusion **47**, R35 (2005).

[6] A. Fujisawa, Nucl. Fusion **49**, 013001 (2009).

[7] Z. Lin, Science **281**, 1835 (1998).

[8] H. Biglari, P. H. Diamond, and P. W. Terry, Phys. Fluids B **2**, 1 (1990).

[9] W. Dorland, F. Jenko, M. Kotschenreuther, and B. N. Rogers, Phys. Rev. Lett. **85**, 5579 (2000).

[10] F. Jenko, W. Dorland, M. Kotschenreuther, and B. N. Rogers, Phys. Plasmas **7**, 1904 (2000).

[11] C. Connaughton, S. Nazarenko, and B. Quinn, Phys. Rep. **604**, 1 (2015).

[12] J. C. Hillesheim, E. Delabie, H. Meyer, C. F. Maggi, L. Meneses, E. Poli, and JET Contributors, Phys. Rev. Lett. **116**, 065002 (2016).

[13] G. D. Conway, B. Scott, J. Schirmer, M. Reich, A. Kendl, and t. A. U. Team, Plasma Phys. Control. Fusion **47**, 1165 (2005).

[14] A. R. Vasavada and A. P. Showman, Rep. Prog. Phys. **68**, 1935 (2005).

[15] J. A. Krommes, Phys. Rep. **360**, 1 (2002).

[16] R. H. Kraichnan, *The Closure Problem of Turbulence Theory* (Hardpress, 2013).

[17] J. C. Bowman, J. A. Krommes, and M. Ottaviani, Phys. Fluids B **5**, 3558 (1993).

[18] P. C. Martin, E. D. Siggia, and H. A. Rose, Phys. Rev. A **8**, 423 (1973).

[19] B. F. Farrell and P. J. Ioannou, J. Atmos. Sci. **60**, 2101 (2003).

[20] B. F. Farrell and P. J. Ioannou, J. Atmos. Sci. **64**, 3652 (2007).

[21] B. F. Farrell and P. J. Ioannou, Phys. Plasmas **16**, 112903 (2009).

[22] K. Srinivasan and W. R. Young, J. Atmos. Sci. **69**, 1633 (2012).

[23] J. B. Parker and J. A. Krommes, Phys. Plasmas **20**, 100703 (2013).

[24] D. E. Ruiz, J. B. Parker, E. L. Shi, and I. Y. Dodin, Phys. Plasmas **23**, 122304 (2016).

[25] H. Zhu, Y. Zhou, D. E. Ruiz, and I. Y. Dodin, Phys. Rev. E **97**, 053210 (2018).

[26] H. Zhu, Y. Zhou, and I. Y. Dodin, Phys. Rev. Lett. **124**, 055002 (2020).

[27] H. Zhu, Y. Zhou, and I. Y. Dodin, J. Plasma Phys. **86**, 905860405 (2020).

[28] J. B. Parker, J. Plasma Phys. **82**, 595820602 (2016).

[29] J. B. Parker, Phys. Plasmas **25**, 055708 (2018).

[30] H. Zhu, Y. Zhou, and I. Y. Dodin, Phys. Plasmas **25**, 072121 (2018).

[31] A. I. Smolyakov and P. H. Diamond, Phys. Plasmas **6**, 4410 (1999).

[32] A. I. Smolyakov, P. H. Diamond, and M. Malkov, Phys. Rev. Lett. **84**, 491 (2000).

[33] M. A. Malkov and P. H. Diamond, Phys. Plasmas **8**, 3996 (2001).

[34] M. A. Malkov, P. H. Diamond, and M. N. Rosenbluth, Phys. Plasmas **8**, 5073 (2001).

[35] P. H. Diamond, Y. M. Liang, B. A. Carreras, and P. W. Terry, Phys. Rev. Lett. **72**, 2565 (1994).

[36] E.-j. Kim and P. H. Diamond, Phys. Rev. Lett. **90**, 185006 (2003).

[37] P. Kaw, R. Singh, and P. H. Diamond, Plasma Phys. Control. Fusion **44**, 51 (2002).

[38] R. Trines, R. Bingham, L. O. Silva, J. T. Mendonça, P. K. Shukla, and W. B. Mori, Phys. Rev. Lett. **94**, 165002 (2005).

[39] R. Singh, R. Singh, P. Kaw, Ö. D. Gürcan, and P. H. Diamond, Phys. Plasmas **21**, 102306 (2014).

[40] H. Zhu, Y. Zhou, and I. Y. Dodin, Phys. Plasmas **25**, 082121 (2018).

[41] H. Weyl, *The Theory of Groups and Quantum Mechanics* (Dover, New York, 1931).

[42] E. Wigner, Phys. Rev. **40**, 749 (1932).

[43] S. W. McDonald, Phys. Rep. **158**, 337 (1988).

[44] E. R. Tracy, A. J. Brizard, A. S. Richardson, and A. N. Kaufman, *Ray Tracing and Beyond: Phase Space Methods in Plasma Wave Theory* (Cambridge University Press, New York, 2014).

[45] D. E. Ruiz, Ph.D. thesis, Princeton University, Princeton (2017).

[46] G. B. Whitham, *Linear and Nonlinear Waves* (Wiley, New York, 2011).

[47] J. A. Krommes and C.-B. Kim, Phys. Rev. E **62**, 8508 (2000).

[48] V. Tsiolis, Y. Zhou, and I. Y. Dodin, Phys. Lett. A **384**, 126377 (2020).

[49] J. Squire and A. Bhattacharjee, Phys. Rev. Lett. **114**, 085002 (2015).

[50] G. B. Whitham, Proc. Roy. Soc. Lond. A **283**, 238 (1965).

[51] R. M. Miura and M. D. Kruskal, SIAM J. Appl. Math. **26**, 376 (1974).

[52] D. D. Holm, J. E. Marsden, and T. S. Ratiu, Adv. Math **137**, 1 (1998).

[53] G. B. Whitham, J. Fluid Mech. **22**, 273 (1965).

[54] G. B. Whitham, *Linear and Nonlinear Waves*, Whitham/Linear (John Wiley & Sons, Inc., Hoboken, NJ, USA, 1999).

[55] N. Fenichel, J. Differ. Eq. **31**, 53 (1979).

[56] F. Verhulst, *Methods and Applications of Singular Perturbations*, vol. 50 of *Boundary Layers and Multiple Timescale Dynamics* (Springer-Verlag, New York, 2005), 1st ed.

[57] A. J. Harvey-Thompson, M. R. Weis, E. C. Harding, M. Geissel, D. J. Ampleford, G. A. Chandler, J. R. Fein, M. E. Glinsky, M. R. Gomez, K. D. Hahn, et al., Phys. Plasmas **25**, 112705 (2018).

[58] A. J. Harvey-Thompson, M. Geissel, C. A. Jennings, M. R. Weis, M. R. Gomez, J. R. Fein, D. J. Ampleford, G. A. Chandler, M. E. Glinsky, K. D. Hahn, et al., Phys. Plasmas **26**, 032707 (2019).

[59] I. Y. Dodin and N. J. Fisch, Phys. Rev. Lett. **112**, 205002 (2014).

[60] D. E. Ruiz, C. L. Ellison, and I. Y. Dodin, Phys. Rev. A **92**, 062124 (2015).

[61] D. E. Ruiz and I. Y. Dodin, Phys. Rev. A **95**, 032114 (2017).

[62] I. Y. Dodin and D. E. Ruiz, J. Plasma Phys. **83**, 905830201 (2017).

[63] H. C. Watkins and R. J. Kingham, Phys. Plasmas **25**, 092701 (2018).

[64] I. Y. Dodin and A. V. Arefiev, Phys. Plasmas **24**, 032119 (2017).

[65] D. E. Ruiz and I. Y. Dodin, Phys. Lett. A **379**, 2337 (2015).

[66] D. E. Ruiz and I. Y. Dodin, Phys. Plasmas **24**, 055704 (2017).

[67] I. Y. Dodin, D. E. Ruiz, and S. Kubo, Phys. Plasmas **24**, 122116 (2017).

[68] D. D. Ryutov, M. S. Derzon, and M. K. Matzen, Rev. Mod. Phys. **72**, 167 (2000).

[69] M. G. Haines, Plasma Phys. Control. Fusion **53**, 093001 (2011).

[70] P. M. Bellan, *Fundamentals of plasma physics* (Cambridge University Press, Cambridge, 2012).

[71] D. B. Sinars, M. A. Sweeney, C. S. Alexander, D. J. Ampleford, T. Ao, J. P. Apruzese, C. Aragon, D. J. Armstrong, K. N. Austin, T. J. Awe, et al., Phys. Plasmas **27**, 070501 (2020).

[72] S. A. Slutz and R. A. Vesey, Phys. Rev. Lett. **108**, 1139 (2012).

[73] S. A. Slutz, M. C. Herrmann, R. A. Vesey, A. B. Sefkow, D. B. Sinars, D. C. Rovang, K. J. Peterson, and M. E. Cuneo, Phys. Plasmas **17**, 056303 (2010).

[74] A. B. Sefkow, S. A. Slutz, J. M. Koning, M. M. Marinak, K. J. Peterson, D. B. Sinars, and R. A. Vesey, Phys. Plasmas **21**, 072711 (2014).

[75] M. R. Gomez, S. A. Slutz, A. B. Sefkow, D. B. Sinars, K. D. Hahn, S. B. Hansen, E. C. Harding, P. F. Knapp, P. F. Schmit, C. A. Jennings, et al., Phys. Rev. Lett. **113**, 155003 (2014).

[76] P. F. Knapp, M. R. Martin, D. H. Dolan, K. Cochrane, D. Dalton, J. P. Davis, C. A. Jennings, G. P. Loisel, D. H. Romero, I. C. Smith, et al., Phys. Plasmas **24**, 042708 (2017).

[77] D. B. Sinars, S. A. Slutz, M. C. Herrmann, R. D. McBride, M. E. Cuneo, K. J. Peterson, R. A. Vesey, C. Nakhleh, B. E. Blue, K. Killebrew, et al., Phys. Rev. Lett. **105**, 185001 (2010).

[78] D. B. Sinars, S. A. Slutz, M. C. Herrmann, R. D. McBride, M. E. Cuneo, C. A. Jennings, J. P. Chittenden, A. L. Velikovich, K. J. Peterson, R. A. Vesey, et al., Phys. Plasmas **18**, 056301 (2011).

[79] R. D. McBride, M. R. Martin, R. W. Lemke, J. B. Greenly, C. A. Jennings, D. C. Rovang, D. B. Sinars, M. E. Cuneo, M. C. Herrmann, S. A. Slutz, et al., Phys. Plasmas **20**, 056309 (2013).

[80] T. J. Awe, K. J. Peterson, E. P. Yu, R. D. McBride, D. B. Sinars, M. R. Gomez, C. A. Jennings, M. R. Martin, S. E. Rosenthal, D. G. Schroen, et al., Phys. Rev. Lett. **116**, 956 (2016).

[81] T. J. Awe, R. D. McBride, C. A. Jennings, D. C. Lamppa, M. R. Martin, D. C. Rovang, S. A. Slutz, M. E. Cuneo, A. C. Owen, D. B. Sinars, et al., Phys. Rev. Lett. **111**, 956 (2013).

[82] D. A. Yager-Elorriaga, P. Zhang, A. M. Steiner, N. M. Jordan, P. C. Campbell, Y. Y. Lau, and R. M. Gilgenbach, Phys. Plasmas **23**, 124502 (2016).

[83] D. A. Yager-Elorriaga, P. Zhang, A. M. Steiner, N. M. Jordan, Y. Y. Lau, and R. M. Gilgenbach, Phys. Plasmas **23**, 101205 (2016).

[84] J. C. Zier, R. M. Gilgenbach, D. A. Chalenski, Y. Y. Lau, D. M. French, M. R. Gomez, S. G. Patel, I. M. Rittersdorf, A. M. Steiner, M. Weis, et al., Phys. Plasmas **19**, 032701 (2012).

[85] M. D. Kruskal and M. Schwarzschild, Proc. R. Soc. Lond. A. **223**, 348 (1954).

[86] S. Chandrasekhar, *Hydrodynamic and hydromagnetic stability*, Oxford University Press, London (1961).

[87] E. G. Harris, Phys. Fluids **5**, 1057 (1962).

[88] Y. Y. Lau, J. C. Zier, I. M. Rittersdorf, M. R. Weis, and R. M. Gilgenbach, Phys. Rev. E **83**, 066405 (2011).

[89] M. R. Weis, P. Zhang, Y. Y. Lau, I. M. Rittersdorf, J. C. Zier, R. M. Gilgenbach, M. H. Hess, and K. J. Peterson, Phys. Plasmas **21**, 122708 (2014).

[90] A. B. Bud'ko, F. S. Felber, A. I. Kleev, M. A. Liberman, and A. L. Velikovich, Phys. Fluids B **1**, 598 (1989).

[91] M. R. Weis, P. Zhang, Y. Y. Lau, P. F. Schmit, K. J. Peterson, M. Hess, and R. M. Gilgenbach, Phys. Plasmas **22**, 032706 (2015).

[92] X. Yang, D.-L. Xiao, N. Ding, and J. Liu, Chin. Phys. B **26**, 075202 (2017).

[93] Y. B. Sun and A. R. Piriz, Phys. Plasmas **21**, 072708 (2014).

[94] S. A. Piriz, A. R. Piriz, and N. A. Tahir, J. Fluid Mech. **867**, 1012 (2019).

[95] S. A. Piriz, A. R. Piriz, and N. A. Tahir, Phys. Fluids **30**, 111703 (2018).

[96] W. Zhang, Z. Wu, and D. Li, Phys. Plasmas **12**, 042106 (2005).

[97] P. Zhang, Y. Y. Lau, I. M. Rittersdorf, M. R. Weis, R. M. Gilgenbach, D. Chalenski, and S. A. Slutz, Phys. Plasmas **19**, 022703 (2012).

[98] D. D. Ryutov, T. J. Awe, S. B. Hansen, R. D. McBride, K. J. Peterson, D. B. Sinars, and S. A. Slutz, in *AIP Conf. Proc.* (AIP Publishing LLC, Napa, 2015), pp. 63–66.

[99] A. L. Velikovich and P. F. Schmit, Phys. Plasmas **22**, 122711 (2015).

[100] P. F. Schmit, A. L. Velikovich, R. D. McBride, and G. K. Robertson, Phys. Rev. Lett. **117**, 205001 (2016).

[101] J. D. Huba, Phys. Plasmas **3**, 2523 (1996).

[102] D. L. Peterson, R. L. Bowers, J. H. Brownell, A. E. Greene, K. D. McLenithan, T. A. Oliphant, N. F. Roderick, and A. J. Scannapieco, Phys. Plasmas **3**, 368 (1996).

[103] M. R. Douglas, C. Deeney, and N. F. Roderick, Phys. Plasmas **5**, 4183 (1998).

[104] C. E. Seyler, M. R. Martin, and N. D. Hamlin, Phys. Plasmas **25**, 062711 (2018).

[105] E. Ott, Phys. Rev. Lett. **29**, 1429 (1972).

[106] M. M. Basko, Phys. Plasmas **1**, 1270 (1994).

[107] Y. A. Bashilov and S. V. Pokrovskii, Sov. Phys. Tech. Phys. **22**, 1306 (1977).

[108] M. P. Desjarlais and B. M. Marder, Phys. Plasmas **6**, 2057 (1999).

[109] D. D. Ryutov and M. A. Dorf, Phys. Plasmas **21**, 112704 (2014).

[110] D. E. Ruiz and I. Y. Dodin, Phys. Lett. A **379**, 2623 (2015).

[111] D. E. Ruiz and I. Y. Dodin, Phys. Rev. A **92**, 043805 (2015).

[112] J. C. Luke, J. Fluid Mech. **27**, 395 (1967).

[113] R. L. Ingraham, Proc. Phys. Soc. B **67**, 748 (1954).

[114] J. W. Jacobs and I. Catton, J. Fluid Mech. **187**, 329 (1988).

[115] W. H. Liu, L.-F. Wang, W.-H. Ye, and X. T. He, Phys. Plasmas **19**, 042705 (2012).

[116] L.-F. Wang, J.-F. Wu, W.-H. Ye, W.-Y. Zhang, and X. T. He, Phys. Plasmas **20**, 042708 (2013).

[117] L.-F. Wang, H.-Y. Guo, J.-F. Wu, W.-H. Ye, J. Liu, W.-Y. Zhang, and X. T. He, Phys. Plasmas **21**, 122710 (2014).

[118] L.-F. Wang, J.-F. Wu, H.-Y. Guo, W.-H. Ye, J. Liu, W.-Y. Zhang, and X. T. He, Phys. Plasmas **22**, 082702 (2015).

[119] H.-Y. Guo, L.-F. Wang, W.-H. Ye, J.-F. Wu, and W.-Y. Zhang, Chinese Phys. Lett. **34**, 045201 (2017).

[120] J. Zhang, L.-F. Wang, W.-H. Ye, J.-F. Wu, H.-Y. Guo, Y. K. Ding, W.-Y. Zhang, and X. T. He, Phys. Plasmas **25**, 082713 (2018).

[121] M. Berning and A. M. Rubenchik, Phys. Fluids **10**, 1564 (1998).

[122] S. Atzeni and J. Meyer-ter Vehn, *The Physics of Inertial Fusion: BeamPlasma Interaction, Hydrodynamics, Hot Dense Matter*, International Series of Monographs on Physics (Oxford University Press Inc., New York, 2009).

[123] P. F. Knapp, M. R. Martin, D. Yager-Elorriaga, A. J. Porwitzky, F. W. Doss, G. A. Shipley, C. A. Jennings, D. E. Ruiz, T. Byvank, C. C. Kuranz, et al., Phys. Plasmas **27**, 092707 (2020).

[124] M. R. Gomez, S. A. Slutz, P. F. Knapp, K. D. Hahn, M. R. Weis, E. C. Harding, M. Geissel, J. R. Fein, M. E. Glinsky, S. B. Hansen, et al., IEEE Trans. Plasma Sci. **47**, 2081 (2019).

[125] P. F. Knapp, M. R. Gomez, S. B. Hansen, M. E. Glinsky, C. A. Jennings, S. A. Slutz, E. C. Harding, K. D. Hahn, M. R. Weis, M. Evans, et al., Phys. Plasmas **26**, 012704 (2019).

[126] P. F. Schmit, P. F. Knapp, S. B. Hansen, M. R. Gomez, K. D. Hahn, D. B. Sinars, K. J. Peterson, S. A. Slutz, A. B. Sefkow, T. J. Awe, et al., Phys. Rev. Lett. **113**, 155004 (2014).

[127] P. F. Knapp, P. F. Schmit, S. B. Hansen, M. R. Gomez, K. D. Hahn, D. B. Sinars, K. J. Peterson, S. A. Slutz, A. B. Sefkow, T. J. Awe, et al., Phys. Plasmas **22**, 056312 (2015).

[128] S. A. Slutz, W. A. Stygar, M. R. Gomez, K. J. Peterson, A. B. Sefkow, D. B. Sinars, R. A. Vesey, E. M. Campbell, and R. Betti, Phys. Plasmas **23**, 022702 (2016).

[129] R. D. McBride and S. A. Slutz, Phys. Plasmas **22**, 052708 (2015).

[130] S. A. Slutz, Phys. Plasmas **25**, 082707 (2018).

DISTRIBUTION

Hardcopy—External

Number of Copies	Name(s)	Company Name and Company Mailing Address

Hardcopy—Internal

Number of Copies	Name	Org.	Mailstop
1	Daniel E. Ruiz	1684	1186
1	D. Chavez, LDRD Office	1911	0359

Email—Internal (encrypt for OUO)

Name	Org.	Sandia Email Address
Technical Library	01177	libref@sandia.gov

Sandia National Laboratories is a multimission laboratory managed and operated by National Technology & Engineering Solutions of Sandia LLC, a wholly owned subsidiary of Honeywell International Inc., for the U.S. Department of Energy's National Nuclear Security Administration under contract DE-NA0003525.